UQAC
Université du Québec
à Chicoutimi

Geology of the Western Part of the Porphyry Zone, Douay Gold Deposit: Genesis of Archean 'syenite-associated' mineralization in the Northern Abitibi Greenstone Belt

Géologie de la partie ouest de la zone porphyrique, gisement aurifère Douay : genèse de la minéralisation archéenne 'associée à la syénite' dans la ceinture de roches vertes du nord de l'Abitibi

Par

Taylor Wasuita

Sous la direction de Dominique Genna (UQAC), Ross Sherlock (LU), Benoît Dubé (CGC), Fred Speidel (Maple Gold Mines Ltd.)

Mémoire présenté à l'Université du Québec à Chicoutimi en vue de l'obtention du grade de Maîtrise ès sciences appliquées (M. Sc. A.) en géologie et génie géologique

Québec, Canada

RÉSUMÉ

Dans la ceinture de roches vertes de l'Abitibi, le rôle des intrusions alcalines dans la formation des gisements d'or associés aux syénites reste débattu. Ce manque de consensus affecte les stratégies d'exploration basées sur le modèle métallogénique des dépôts d'or liés aux intrusions (IRGS). Le gisement de Douay est un IRGS archéen, également appelé minéralisation aurifère associée aux syénites, situé dans la partie nord de la ceinture de roches vertes de l'Abitibi, à 55 km au sud-ouest de Matagami, Québec. Le gisement appartient à Maple Gold Mines Ltd. et contient 8,6 Mt de ressources minérales indiquées à une teneur moyenne de 1,52 g/t Au, et 71,2 Mt de ressources minérales inférées à une teneur moyenne de 1,03 g/t Au. Ce gisement est situé à proximité de la zone tectonique de Casa Berardi (CBTZ). La lithologie à Douay se compose de trois principaux Groupes : le Groupe de Cartwright Hills (2721 Ma), le Groupe de Taibi (<2969 Ma) et le complexe intrusif alcalin de Douay (2676 Ma) qui est spatialement associé à la minéralisation aurifère. Le gisement de Douay est un exemple de projet d'exploration reposant sur un modèle métallogénique débattu, c'est-à-dire que la minéralisation aurifère est spatialement associée à la syénite de Douay et peut correspondre à un IRGS mais est également un dépôt contrôlé structurellement qui peut correspondre à un système aurifère orogénique hébergé par une intrusion. Cette étude se concentre sur les caractéristiques géologiques de la partie occidentale de la zone porphyrique du gisement aurifère de Douay afin de fournir des contraintes sur le modèle métallogénique IRGS. Ce projet contribue également à évaluer si les magmas alcalins archéens ont le potentiel de contribuer des quantités significatives de fluides porteurs d'or aux systèmes minéralisateurs néoarchéens.

La zone porphyrique occidentale héberge un complexe alcalin multiphase largement métasomatisé. La minéralisation aurifère tend à être spatialement associée aux roches les plus altérées du complexe intrusif alcalin de Douay. Le complexe alcalin de Douay se compose de quatre phases : 1) faciès albitisé, 2) faciès hématisé, 3) faciès carbonatisé, 4) faciès intrusif riche en ça. Le complexe intrusif alcalin de Douay (DAIC) présente une signature polymétallique (Au, Ag, Te, Pb, Cu et Bi). La signature en éléments traces des grains de pyrite affiche une similarité entre les faciès albitisé, hématisé et carbonatisé, suggérant qu'ils font partie d'un seul système magmatique-hydrothermal évolutif. La signature en éléments traces de la pyrite est très différente des systèmes orogéniques, mais similaire à d'autres IRGS situés dans la sous-province de l'Abitibi. Les inclusions de barytine, observées dans le bord et le cœur de la pyrite, et l'enrichissement en Te suggèrent que la minéralisation s'est formée à partir d'une source de fluide magmatique oxydé. Cette étude contribuera à notre compréhension du rôle des intrusions magmatiques alcalines dans les processus de minéralisation et de leurs différences par rapport aux systèmes aurifères orogéniques. Elle fournira des informations précieuses pour les stratégies d'exploration et fera progresser nos connaissances sur la fertilisation de la croûte supérieure néoarchéenne.

ABSTRACT

In the Abitibi greenstone belt, the role played by the alkaline intrusions in the formation of syenite-associated gold deposits remains debated. This lack of consensus affects exploration strategies based on the intrusion-related gold deposits (IRGS) metallogenic model. The Douay deposit is an Archean IRGS, also referred to as a syenite-associated gold mineralization, located in the northern part of the Abitibi greenstone belt, 55 km southwest of Matagami, Québec. The deposit is owned by Maple Gold Mines Ltd. and contains 8.6 Mt of indicated mineral resources at an average grade of 1.52 g/t Au, and 71.2 Mt of inferred mineral resources at an average grade of 1.03 g/t Au. This deposit is located within close proximity to the Casa Berardi Tectonic Zone (CBTZ). The lithology at Douay consists of three main groups: the volcanic Cartwright Hills Group (2721 Ma), the sedimentary Taibi Group (<2969 Ma), and the Douay Alkaline Intrusive Complex (2676 Ma) that is spatially associated with gold mineralization. The Douay deposit is an example of an exploration project that has a debated metallogenic model, i.e., gold mineralization is spatially associated with the Douay syenite and may correspond to an IRGS but is also a structurally controlled deposit that may correspond to an intrusion-hosted orogenic gold system (OGS). This study focuses on the geological characteristics of the western portion of the Porphyry Zone of the Douay Gold deposit to provide constraints on the metallogenic model. This project also contributes to evaluate if Archean alkaline magmas have the potential to contribute significant amounts of gold-bearing fluids to Neoarchean mineralizing systems.

The western porphyry zone hosts an extensively metasomatized multiphase intrusive alkaline complex. The gold mineralization tends to be spatially associated with the most altered rocks of the Douay Alkaline Intrusive Complex. The Douay Alkaline Intrusive Complex consists of four phases: 1) albitized facies, 2) hematized facies, 3) carbonatized facies, 4) Ca-rich intrusive facies. The Douay Alkaline Intrusive Complex exhibits a polymetallic signature (Au, Ag, Te, Pb, Cu, and Bi). The trace element signature of the pyrite grains displays a similar signature between the albitized, hematized, and carbonatized facies suggesting that they are part of a single evolving magmatic-hydrothermal system. The trace element signature of pyrite is very different from orogenic systems, but similar to other IRGS located in the Abitibi subprovince. Barite inclusions, observed in the rim and the core of pyrite and Te-enrichment suggests that mineralization formed from an oxidized magmatic fluid source. This study will contribute to our understanding of the role of alkaline magmatic intrusions in mineralizing processes and their differences from orogenic gold systems. It will provide valuable insights for exploration strategies and advance our knowledge of Neoarchean upper crustal fertilization.

Table of Contents

LIST OF FIGURES

LIST OF TABLES

LIST OF ANNEXES

Annex 1: Total Mineral Resources Table

Annex 2: Collar Location Information

Annex 3: Sample Summary Table

Electronic Supplementary Material (5 Excel Files)

Supplementary Information #1A-E Sample information
S1A. Sample Information
S1B. Hand Sample Descriptions
S1C. Modal Proportions
S1D. Whole-rock Geochemical Data
S1E. Scanning Electron Microprobe (SEM) Database
Supplementary Information #2A-H Microprobe Data
S2A. Apatite
S2B. Amphibole
S2C. Carbonate
S2D. Feldspar
S2E. Fluorite
S2F. Gold
S2G. Muscovite
S2H. Sulfides
Supplementary Information #3A-F LA-ICP-MS Pyrite QA/QC standards
S3. Pyrite QA/QC
Supplementary Information #4 - LA-ICP-MS Pyrite Results
S4A. Pyrite Detection Limits
S4B. LA-ICP-MS Pyrite Results
S4C. Pyrite Median Values
S4D. Pyrite Median Values Diagrams
Supplementary Information #5A-D LA-ICP-MS Carbonates & Feldspars
S5A. Carbonate Detection Limits
S5B. LA-ICP-MS Carbonates
S5C. Feldspar Detection Limits
S5D. LA-ICP-MS Feldspar Results

LIST OF ABBREVIATIONS

Alb: Albite
Au: Native Gold
Any: Anhydrite
Ba: Barite
BSE: Back-Scattered Electron
Cb: Carbonate
CL: Cathodoluminescence
Cpy: Chalcopyrite
Chl: Chlorite
DAIC: Douay Alkaline Intrusive Complex
EDS: Energy Dispersive Spectroscopy
EMPA: Electron Microprobe
Fsp: Feldspar
Fl: Fluorite
Hem: Hematite
HREE: Heavy Rare Earth Elements
IRGS: Intrusion Related Gold Systems
LabMaTer: Laboratoire des matériaux terrestres
LA-ICP-MS: Laser-ablation induced-coupled plasma mass spectrometer
LOD: Limit of Detection
LOI: Loss on ignition
LREE: Light Rare Earth Elements
Mol: Molybdenite
OGS: Orogenic Gold Systems
PPL: Plane Polarized Light
Py: Pyrite
QA-QC: Quality Assurance-Quality Control
Qtz: Quartz
REE: Rare-Earth Elements
SEM: Scanning Electron Microprobe
Spec: Specularite
TAS : Total Alkali Silicate
UQAC : Université du Québec à Chicoutimi
XP: Cross Polarized Light

REMERCIEMENTS

I would like to express my deepest gratitude to everyone who supported and guided me throughout this MSc journey. This work would not have been possible without the support of Dominique Genna (UQAC), Lucie Mathieu, Ross Sherlock, Benoît Dubé, Fred Speidel, Maria Sokolov, Pavel Sokolov, and Josh Pelletier for their insightful guidance, continuous encouragement, and invaluable contributions.

First and foremost, I would like to thank my current supervisor, Dominique Genna. Your expertise and mentorship have been instrumental in shaping my research and academic growth. I am also grateful to Lucie Mathieu for providing me with this opportunity. Also, I would like to thank Maple Gold Mines Ltd. for making me feel welcome when coming to site, guiding and mentoring me, and teaching me about this fascinating deposit.

I am immensely thankful to the Metal Earth project, led by the Mineral Exploration Research Center (MERC) at the Harquail School of Earth Sciences, Laurentian University, ON, for funding this project. Their financial assistance provided the necessary resources for the successful completion of this research. Special thanks to Ross Sherlock for his assistance and collaboration.

Additionally, I extend my appreciation to my colleagues and fellow researchers at the University of Québec in Chicoutimi (UQAC) and Laurentian University (LU). Their feedback, discussions, and camaraderie enriched my research experience. I also thank my examiners for both my research proposal (Lucie Mathieu, Ross Sherlock, Réal Daigneault, Pedro Jugo, and Romain Chesnaux), and my final manuscript review (Michel Jébrak and Sarah Dare) for their valuable insights and comments.

I would like to personally thank Pape Doudou Tague for his support during the cathodoluminescence (CL8200 Mk5-1 Optical) analyses and Audrey Lavoie for her assistance with the LA-ICP-MS analyses at UQAC. I also extend my gratitude to the Mineral Exploration Research Centre (MERC) laboratory at Laurentian University, Sudbury, ON, Canada, for allowing me to use the Tescan Vega 3 scanning electron microscope (SEM) to obtain all relevant SEM data.

Finally, I would like to thank my family, partner, and friends for their patience, understanding, and unwavering belief in me. Your support has been my foundation throughout this journey.

CHAPTER 1: INTRODUCTION

In the Neoarchean supracrustal rocks located in the Abitibi greenstone belt (Fig. 1), Superior craton, Canada, gold mineralization is often associated with structural traps along regional deformation zones (McCuaig and Kerrich, 1998). Orogenic gold systems (OGS) are the most abundant type of Archean gold deposit found in the Abitibi greenstone belt (Goldfarb & Groves, 2015; Dubé & Mercier-Langevin, 2020). Orogenic gold systems (OGS) are defined as structurally controlled deposits formed by the circulation of metamorphic fluids generated by the metamorphic devolatilization of basalts and/or sedimentary rocks during large scale compressional events at convergent plate margins (Groves et al., 1998). Although, some Archean gold deposits are associated with oxidized alkaline intrusions emplaced syn to post-collisional tectonic settings, which are described using an Intrusion-Related Gold Systems (IRGS) model (Rowins et al., 1993, Stünitz and Fitz Gerald, 1993, Robert, 2001, Ispolatov et al., 2008). Archean IRGS, as described by Robert (2001), are structurally controlled magmatic-hydrothermal systems that are genetically associated with oxidized alkaline intrusions that exsolve metal-bearing magmatic fluids as they crystallize. However, the relationship between gold mineralization and syn- to post-tectonic alkaline intrusions has been long debated in the Abitibi subprovince at deposits such as Beattie (Bigot and Jébrak, 2015), Lac Bachelor (Fayol and Jébrak, 2017), Wasamac (Mériaud and Jébrak, 2017), Upper Beaver (Kontak et al., 2008), Kirkland Lake (Ispolatov et al., 2008), and Canadian Malartic (Helt et al., 2014, De Souza et al., 2015 & 2019).

Orogenic gold systems and intrusion-related gold systems, however, display notable differences in their deposit characteristics. In the Abitibi greenstone belt, large volumes of metamorphic fluids are produced during the main shortening event (Groves et al., 1998, Dubé and Gosselin, 2007; Dubé and Mercier-Langevin, 2020). Metamorphic fluids are channelized by crustal-scale faults, and these fluids transport and release gold in mesozonal conditions (Groves et al.,1998). The metamorphic fluids tend to be reduced, CO_2-rich, and low-salinity (Groves et al., 1998, Phillips and Powell, 2010, Goldfarb and Groves, 2015). The mineralization is typically hosted by laminated quartz-carbonate reverse-oblique veins and associated shallow dipping extensional veins. In contrast, IRGS are structurally controlled magmatic-hydrothermal gold mineralizing systems associated with alkaline intrusions that tend to be affected by the main deformation event in the Abitibi subprovince (Robert, 2001, Mathieu, 2021). For IRGS, the mineralizing fluid is oxidized and high temperature, i.e., it can generate potassic metasomatism and hematization (Robert, 2001). These intrusive systems correspond to dyke swarms and small volume intrusions, e.g., the Beattie syenite, which has a surface area of 1.2 km^2 and was emplaced in the upper crust near crustal-scale faults (Robert, 2001, Bigot and Jébrak, 2015). The mineralization also generally displays a polymetallic signature, e.g., the Upper Beaver (Au-Ag-Hg-Te-Bi-Sb; Kontak et al., 2008), Wasamac (W-Pb-Bi-Te-Mo-Ag; Mériaud and Jébrak, 2017), and Beattie (Te-Hg-Mo-As-Au-Se-Ag-Sb; (Bigot and Jébrak, 2015).

This thesis focuses on the geological and geochemical characteristics of the western portion of the Porphyry Zone of the Douay Gold deposit to provide constraints on the timing and genesis of the deposit. The western Porphyry Zone is a representative zone of the Douay Alkaline Intrusive Complex where gold mineralization is mainly hosted in the intrusive phases, but also located along a major deformation zone, the Casa Berardi Tectonic Zone, making this deposit an ideal case study to investigate the hydrothermal contributions from both metamorphic (OGS) and magmatic systems (IRGS). This study contributes to a better understanding of Neoarchean mineralizing systems and the ability for Neoarchean upper crustal fertilizing processes. Furthermore, implications for gold exploration strategies are discussed.

CHAPTER 2: GEOLOGICAL SETTING

2.1 Regional Geology

2.1.1 – Synvolcanic

The Abitibi greenstone belt, located in the southeastern region of Canada's Archean Superior Craton, is dominated by regionally metamorphosed (greenschist facies) supracrustal assemblages (volcanic and sedimentary rocks) and broadly coeval intrusions (Thurston et al., 2008, Monecke et al., 2017b, Dubé and Mercier-Langevin, 2020). The Abitibi greenstone belt was formed by six volcanic events: 1. Pacaud (2750-2735 Ma), 2. Deloro (2734-2724 Ma), 3. Stoughton-Roquemaure (2723-2720 Ma), 4. Kidd-Munro (2720-2710 Ma), 5. Tisdale (2710-2704 Ma), 6. Blake River (2704-2695 Ma; Dubé and Mercier-Langevin, 2020 and references therein). Similar in age and composition to their host volcanic assemblages listed above, synvolcanic intrusions (<2750-2695 Ma) consisted of voluminous tonalite-trondhjemite-granodiorite (TTG) intrusive suites located in the core of major anticlines (Daigneault et al., 1990, Monecke et al., 2017). Volcanic activity was followed by two sedimentary successions: 1. Flysoid sedimentation produced the Taibi (<2700-2685 Ma) and Porcupine assemblages (2690–2685 Ma), which consist of turbidites, conglomerates, and banded iron formations (Ayer et al., 2002, Thurston et al., 2008, Monecke et al., 2017b, Dubé and Mercier-Langevin, 2020). 2. Basin restricted sedimentation characterized by late fluvial-alluvial conglomerates and sandstones forming the Haüy Formation (maximum deposit age of 2692 ± 3 Ma; David et al., 2007) in the northeastern portion of the Abitibi and the Timiskaming Group (<2679-2669 Ma; Ayer et al., 2002) in the south. The Timiskaming Group is a key stratigraphic unit because it forms the youngest Archean supracrustal rocks of the Abitibi greenstone belt and marks one of the earliest appearances of subaerial erosional-depositional conditions (Dubé and Mercier-Langevin, 2020).

2.1.2 – Pre/Syn/Post Timiskaming Intrusions

Intrusions can be classified based on the timing of their emplacement relative to the Timiskaming Group are defined as pre-Timiskaming (post synvolcanic intrusions), early to syn-Timiskaming, and post-Timiskaming (Fig. 1b, Dubé and Mercier-Langevin, 2020). Pre-Timiskaming intrusions (2695 to 2682Ma) can be defined as high-level sub-alkaline (calc-alkaline) quartz-feldspar porphyries ("small plugs") (Dubé and Mercier-Langevin, 2020). These intrusions range in composition from granodiorite to granite, diorite-gabbro, monzodiorite, monzonite, and quartz monzonite (Dubé and Mercier-Langevin, 2020). Examples include the Lower Detour deposit's 2694 Ma feldspar porphyry dike, which contains gold mineralization, and the Main Plug (2685 +/- 3 Ma; Jemielita et al., 1989; Dubé, 2018), which are situated at the Lamaque mine (Castonguay et al., 2020, Dubé and Mercier-Langevin, 2020).

Early to syn-Timiskaming intrusions are alkaline to subalkaline in composition and were emplaced as dikes, plugs, and small stocks. Their compositions range from monzonite to quartz monzonite, and from syenite-to-syenite foidite, with some also containing carbonatite (e.g., Lac Shortt) and lamprophyre (Nadeau et al., 2014; Dubé & Mercier-Langevin, 2020). Several of these intrusions, which host significant gold deposits such as Douay, Young-Davidson, Beattie, and Lac Bachelor, are commonly associated with alteration assemblages such as hematite, albite, sericite, carbonate, and pyrite (Robert, 2001; Zhang et al., 2014; Fayol & Jébrak, 2017; Mériaud & Jébrak, 2017; Dubé & Mercier-Langevin, 2020). These alkaline to subalkaline intrusions are often associated with syn-Hauy fluvial-alluvial deposits in the northern portion of the Abitibi belt and are typically older than their (syn-Timiskaming) counterparts in the southern half of the belt, ranging in age from roughly 2695 to 2688 Ma (Dubé and Mercier-Langevin, 2020). The Douay syenite (2676 +6/–5 Ma; Davis et al., 2000) age is relatively young when compared to other alkaline to subalkaline intrusions in the northern Abitibi greenstone belt, for example Lac Shortt gold deposit (2691 +5/–3Ma carbonatite; Joanisse, 1994; Brisson, 1998). Post-Timiskaming intrusive rocks (~2670Ma) range in composition from granitic, monzogranitic to granodioritic and tend to host no known gold mineralization. They are uncommon in the southern Abitibi and generally form massive, multi-phase batholithic complexes that crosscut the main foliation (Dubé and Mercier-Langevin, 2020).

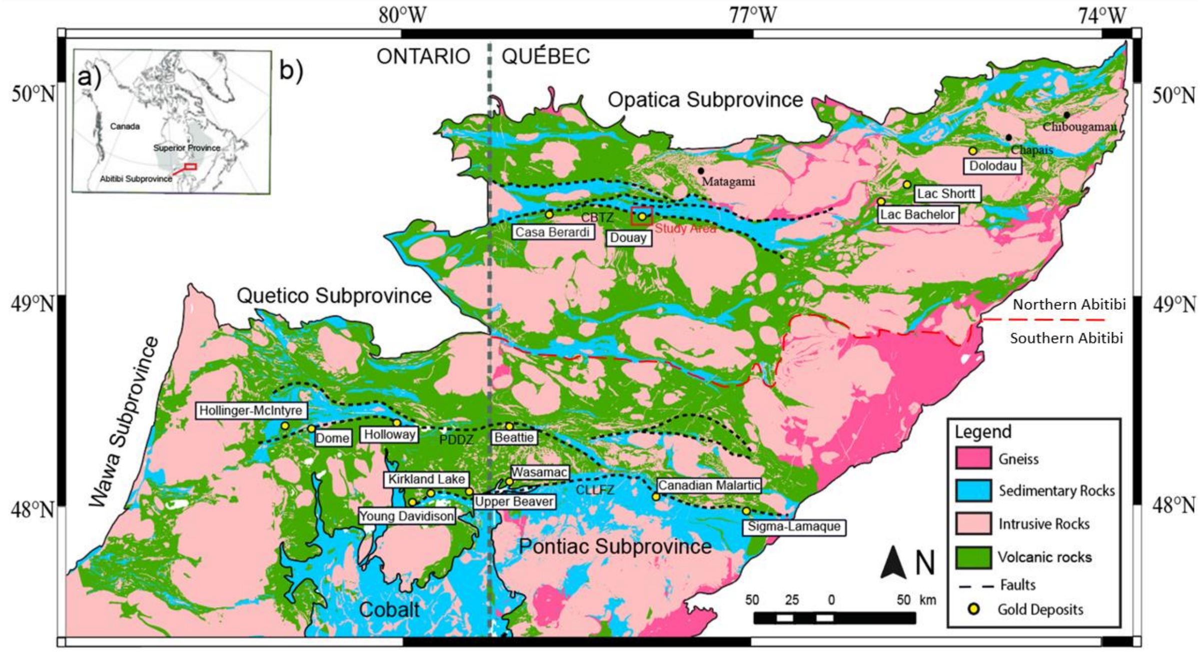

Figure 1: **(a)** Map of Canada displaying the location of Superior province (grey) and the Abitibi subprovince with a red box. **(b)** Generalised geological map of the Abitibi subprovince displaying the distribution of the main lithologies, large scale fault zones such as Cadillac-Larder Lake Fault zone (CLLFZ), Porcupine-Destor Fault Zone (PDFZ), and the Casa Berardi Tectonic Zone (CBTZ), and a selection of significant gold deposits. A red box indicates the location of the Douay gold deposit. The map is modified from the SIGEOM (Système d'Information GÉOMinière) dataset, Ministère des Ressources Naturelles et des Forêts of Québec (MRNF), and from the Ontario Geological Survey (OGS).

2.2 Local Geology of the Douay Gold Deposit

The Douay deposit is located 55 km southwest of the town of Matagami, Québec (Fig. 1b), and it is owned by Maple Gold Mines Ltd. and Agnico Eagle Mines Ltd. The deposit contains 10 Mt of indicated mineral resources at an average grade of 1.59 g/t Au, and 76.7 Mt of inferred mineral resources at an average grade of 1.02 g/t Au (Gosselin, 2020). The Douay deposit is situated along the northern segment of the Casa Berardi Tectonic Zone (CBTZ), an approximately ~80 km long, east-west to northwest trending fault, which separates the Taibi Group to the north from the Cartwright Hills Group to the south (Daigneault et al., 1990, Pilote et al., 1990, El Rassi et al., 2019). The CBDZ is a graphite-bearing fault that contains carbonate-quartz veining (Pilote et al., 1990, El Rassi et al., 2019).

The Cartwright Hills Group (2721.4 ± 3.1 Ma; Legault et al., 2002), is dominated by tholeiitic volcanic rocks (massive and pillow basalts) and coeval gabbro sills, with minor volume of ultramafic lava flows. The Cartwright Hills Group also contains interflow felsic pyroclastic and sedimentary rocks, such as laminated cherts and siltstones (El Rassi et al., 2019). The sedimentary rocks of the Taibi Group uncomfortably overlie the Cartwright Hills Group and correspond to siltstone, mudstone, graywacke, conglomerates, and iron formations. The polygenic conglomerates are dated at <2685 ± 2.6 Ma; Davis et al., 2005) and contain fragments of chert, jasper, mafic and felsic volcanic rocks. The Taibi Group is interpreted to have formed in a deep-water basinal environment toward the end of the synvolcanic period (Dubé and Mercier-Langevin, 2020). The Douay Alkaline Intrusive Complex also hosts part of the mineralization. It consists of monzonitic and syenitic phases, as well as a minor volume of carbonatite intrusions (El Rassi et al., 2019). The monzonitic phase emplaced prior to the syenitic phase, based on a cross-cutting aplite dyke dated at 2690.1 ± 0.96 Ma (Mathieu et al., 2022). The younger syenite phase (2676 +5/-6 Ma; Davis et al., 2000) may be dominant and is comprised of five texturally distinct intrusive units: 1) aphyric syenite; 2) feldspar-porphyritic syenite; 3) aplite dykes; 4) quartz-feldspar-porphyritic syenite; and 5) pegmatite (El Rassi et al., 2019).

The Cartwright Group, Taibi Group, and Douay Alkaline Intrusive Complex are affected by regional foliation and faulting resulting from the D_2-D_3 event (Dubé and Mercier-Langevin, 2020). On the Douay property, several mineralized zones have been identified, including the Douay West Zone, Porphyry Zone, Northwest Zone, Nika Zone, Zone 20, Zone 10, 531 Zone, and Main Zone (Fig. 2a).

The intrusion-hosted mineralization is primarily observed in the Porphyry Zone, where it occurs within and along the margins of the intrusive phases of the Douay Alkaline Intrusive Complex (El Rassi et al., 2019). Structurally controlled mineralization is associated with E- and NW-trending faults, corresponding to the CBDZ, respectively (El Rassi et al., 2019).

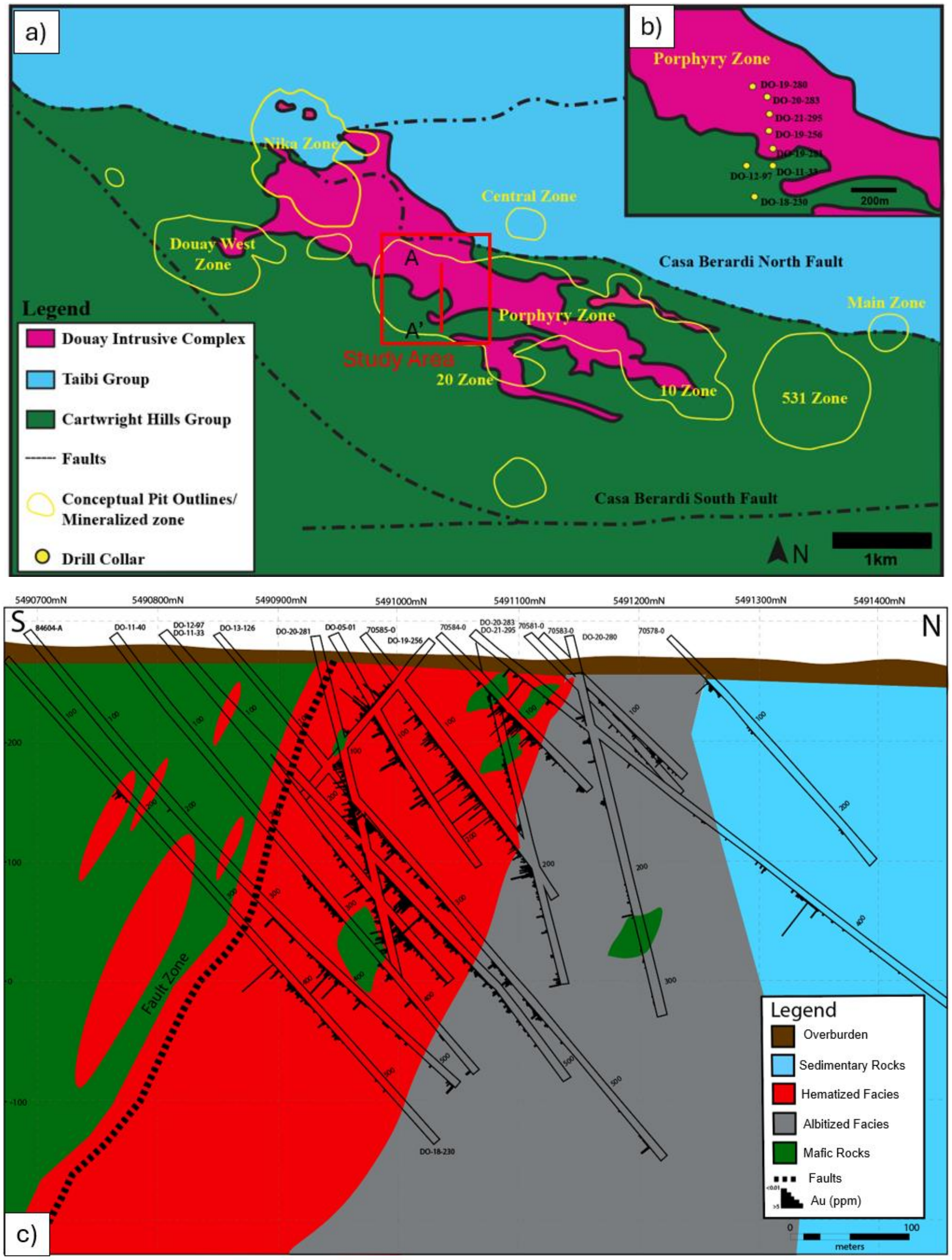

Figure 2: (a) Local geological map of the Douay project showing the main lithological units, location of conceptual pit outlines (yellow) representing mineralized zones, including the main lithological units such as the Douay Alkaline Intrusive Complex (Maple Gold, 2021), **(b)** Represents the locations of eight drillhole collars in the porphyry zone, **(c)** Simplified South to North cross section of the western Porphyry Zone displaying the volcanic and sedimentary rocks along with the different alteration facies of the intrusive complex identified in this project. Gold grades are mainly concentrated throughout the hematized facies with minor gold values observed throughout the albitized facies.

CHAPTER 3: METHODOLOGY

3.1 Sampling

Due to the scarcity of outcrops at the Douay project, drill cores were used to study the Douay Alkaline Intrusive Complex and associated alteration and mineralization. Eight drill holes (DO-11-33, DO-12-97, DO-19-256, DO-20-230, DO-20-280, DO-20-281, DO-20-283, DO-21-295; Fig. 2b) located in the western Porphyry Zone along a N-S transect were selected to document the Porphyry zone deposit. A total of 72 samples were collected from this transect and 5 standard (30 µm) and 67 polished (50 µm) thin sections were produced for petrographic description (Supplementary Information #1). Samples were further characterized using cathodoluminescence (CL8200 Mk5-1 Optical) at UQAC to aid in the identification of different feldspars and carbonate minerals.

3.2 Whole Rock Geochemistry Sampling

Whole-rock analyses were performed on 30 powders left-over from analyses performed between 2012 and 2021 by Maple Gold Mines Ltd. Additional analyses were performed on 12 half-cores samples that correspond to 0.5-1 m long drilled intervals. Powder and rock samples were analyzed by ALS Chemex laboratory. Following four-acid digestion, major elements were analyzed using inductively coupled plasma (ICP) atomic emission spectroscopy (AES), with a detection limit of 0.01 wt%. To analyze trace elements, ICP mass spectrometry (MS) with lithium borate fusion and acid dissolution was used, with detection limits ranging from 0.01 to 5 ppm (Supplementary Information #S1D). To achieve precise and accurate results, rigorous QA-QC methods were strictly followed, including the use of blanks, duplicates, and standards.

3.3 Mineral Chemistry

Mineral chemistry was characterized using the electron microprobe (EMPA) and scanning electron microscope (SEM) instruments. The EMPA instrument was used to analyze feldspars, apatite, fluorite, carbonates, quartz, amphiboles, sulphides, and gold using the CAMECA SX100 microprobe at the Laval University, Québec. The parameters used were a beam current of 20 nA, an accelerating voltage of 15 keV, and beam sizes of 10 and 5 µm. In addition, energy dispersive spectroscopy (EDS) and back-scattered electron (BSE) images were obtained for 12 thin sections and using a Tescan Vega 3 scanning electron microscope (SEM) at the Mineral Exploration Research Centre (MERC) laboratory of Laurentian University, Sudbury, ON, Canada. The SEM instrument was used to gain insights into the chemical composition and textures of the main and accessory minerals (Supplementary Information #S1E).

Laser ablation inductively coupled plasma mass spectrometry (LA-ICP-MS) analyses were conducted on pyrite, as well as on selected feldspar and carbonate grains, from 24 polished thin sections. Analyzes were conducted at the LabMaTer laboratory located in Saguenay, Quebec at UQAC. These in-situ analyses were performed using an Australian Scientific Instrument RESOlution ArF-193 nm excimer laser ablation system outfitted with a double-volume cell S-155 (Laurin Technics) and an Agilent 7900 ICP-MS. The operating parameters are as follows: laser frequency of 15 Hz, dwell time of 5 ms, and energy density of 5 J/cm^2. The minerals and reference materials were analyzed using lines (stage speed = 10 µm/s) with spot sizes of 44 and 54 µm. Analyzes were performed after measuring the gas blank for 20 s.

Twenty-four samples were selected for LA-ICP-MS investigation from the least altered, hematized, albitized, and carbonatized intrusive phases. This study focuses on the distribution of these elements in pyrite: ^{28}Si, ^{29}Si, ^{33}S, ^{34}S, ^{44}Ca, ^{47}Ti, ^{49}Ti, ^{51}V, ^{52}Cr, ^{53}Cr, ^{55}Mn, ^{57}Fe, ^{59}Co, ^{60}Ni, ^{61}Ni,

^{65}Cu, ^{66}Zn, ^{71}Ga, ^{72}Ge, ^{75}As, ^{77}Se, ^{78}Se, ^{82}Se, ^{85}Rb, ^{90}Zr, ^{91}Zr, ^{93}Nb, ^{95}Mo, ^{96}Mo, ^{107}Ag, ^{111}Cd, ^{115}In, ^{118}Sn, ^{121}Sb, ^{125}Te, ^{126}Te, ^{138}Ba, ^{182}W, ^{197}Au, ^{202}Hg, ^{205}Tl, ^{208}Pb, ^{209}Bi. For most elements, the calibration was performed using the UQAC-FeS1 reference material, which is an artificial sulfide produced at UQAC (Savard et al., 2018) based on a technique developed at Kiel University (Garbe-Schönberg and Müller, 2014). The materials MASS-1 (USGS; Wilson et al., 2002), LAFLAMME, NIST610 (Jochum et al., 2011), NIST614 (Jochum et al., 2011), and UQAC-FeS-5 (Savard et al., 2018) are used as quality control reference (Supplementary Information #3).

For carbonates and silicates, Ca, Zr, P, K, Fe, Ni and Al were calibrated using the USGS reference material GSE-1g, which is a fused-basaltic glass containing 10% Fe and 500 ppm of each trace element (Jochum et al., 2005). The materials GSD-3, UQAC-APA, MACS3 (Willson, 2008), GP4, GP6, NIST610 (Jochum et al., 2011), NIST614 (Baker et al., 2004), and NIST616 (Jochum et al., 2011) were used as quality control reference materials (Supplementary Information #3).

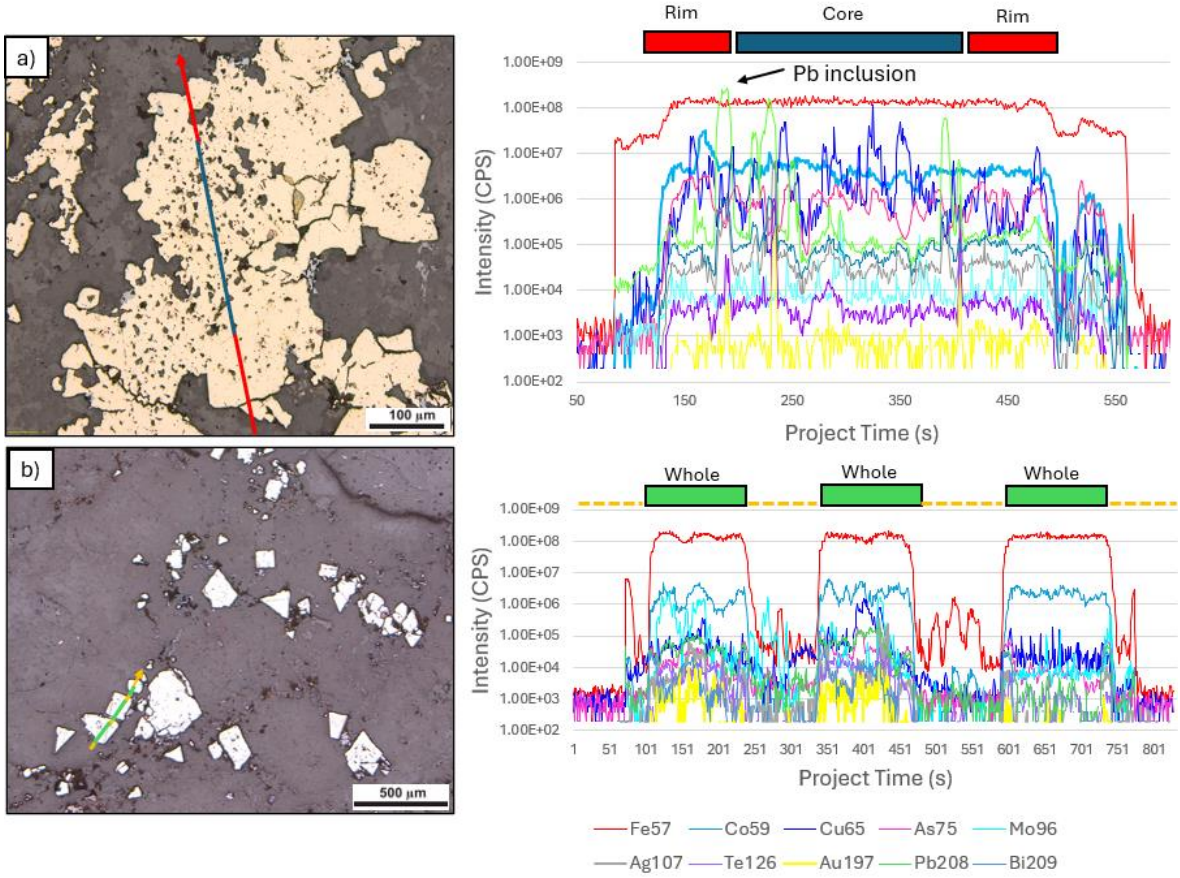

Figure 3: (a) Reflected light image of inclusion rich anhedral pyrite grains from sample TW-72 (DO-21-295 @59.50 m). The line represents the 55 µm wide laser ablation analysis with rim (red) and core (blue) integrations represented on the time-resolved profiles showing the distribution of ^{34}S, ^{57}Fe, ^{59}Co, ^{60}Ni, ^{65}Cu, ^{66}Zn, ^{75}As, ^{96}Mo, ^{107}Ag, ^{126}Te, ^{138}Ba, ^{197}Au, ^{208}Pb, and ^{209}Bi in the pyrite grain, **(b)** Reflected light image of inclusion poor, subhedral pyrite grains from sample TW-66 (DO-20-283 @195.20 m). The line represents the 55 µm wide laser ablation analysis with three whole integrations represented on the time-resolved profiles showing the distribution of ^{34}S, ^{57}Fe, ^{59}Co, ^{60}Ni, ^{65}Cu, ^{66}Zn, ^{75}As, ^{96}Mo, ^{107}Ag, ^{126}Te, ^{138}Ba, ^{197}Au, ^{208}Pb, and ^{209}Bi in the three pyrite grains.

3.3 Reduction of LA-ICP-MS Data

The line analyses were reduced using the LADR 0.6.6.0 software (http://norris.org.au/ladr). For pyrite, the internal standard ^{57}Fe and the stoichiometric value 46.55% (http://webmineral.com) were applied. The QA-QC obtained using external standards is satisfactory (within 10% precision and 15% accuracy for most elements considered in this study; Supplementary Information #3). For pyrite, line analyses were processed as follows: 1) using a single integration for pyrite grains with simple texture; or 2) using two to three integrations for pyrite grains that display texturally distinct core and rim areas. For example, for pyrite grains that display an inclusion-rich core and an inclusion-poor rim (Fig. 3), distinct integrations were performed for the core and rim areas, and single integrations were used for texturally homogeneous grains.

The LADR 0.6.6.0 software (http://norris.org.au/ladr) was also used to reduce the analyzes performed on carbonates and silicates. One integration box per grain is used to characterize the average chemistry of the grains. On a scale smaller than the beam size (54 µm), carbonate and feldspar grains are rich in micro-inclusions. As a result, EDS and EMPA spot analyses were unable to provide satisfactory values for the internal standard. Therefore, the analyses are exported using a generic value of 40.04 wt% Ca for the internal standard. The analyses were then re-calculated to 100% to approximate the average of Ca content of each of the analyzed grains, and the recalculated Ca content was then used as internal standard (^{43}Ca).

CHAPTER 4: RESULTS

4.1 Field Observations and Petrography

The main lithologies observed within the 800 m² study area of the Douay Alkaline Intrusive Complex, located in the western portion of the Porphyry Zone, include basaltic lava flows in the south and sedimentary rocks in the north (Fig. 2). The thin sections are comprised of six lithologies: 1) mafic volcanic rocks 2) sedimentary rocks 3) albitized facies, 4) hematized facies, 5) carbonatized facies, 6) Ca-rich intrusive facies. Each category was identified based on alteration styles deduced from field observations, modal proportions (Supplementary Information #SC1), and SEM results (Supplementary Information #S1E).

4.1.1 Mafic Volcanic Rocks

The mafic volcanic rocks (Fig. 4) distal to the Douay Alkaline Intrusive Complex are basalts from the Cartwright Hills Group (2721.4 ± 3.1 Ma; Legault et al., 2002). They typically range in color from grey to green, are slightly magnetic, and have several different textures, including variolitic (Fig. 4a), pillow, massive (Fig. 4b), and are fine to coarse grained (Fig. 4c). Basalts are composed of albite (15-22 vol%), biotite and chlorite (5-34 vol%), calcite (5-30 vol%, and locally up to 60 vol%), and ± epidote and amphibole (<10 vol%). Chloritization, epidotization, and carbonatization are frequently observed (Fig. 4a). The basalts proximal to the DACIC are grey to green with patchy red sections identified and associated with increased carbonatization, hematization, and potassic alteration (Fig. 4d). Also, 2 to <10cm pink to red syenite and white to grey carbonate rich dyklets commonly crosscut the fine-grained basalts. The contact between the basalts and Douay Alkaline Intrusive Complex is zoned (Fig. 4e), varying between 2-10 m and is marked by a sharp upper and lower contact, characterized by weak to moderate foliation, and a distinct patchy orange red color due to intense potassic, hematitic, and carbonate alteration (Fig. 4e). In thin section the contact contains alkali feldspar (20-25 vol %), albite (20-25 vol%), biotite and chlorite (3-5 vol%), calcite (40-45 vol%), and traces of fine-grained pyrite.

4.1.2 Sedimentary Rocks

The sedimentary rocks are observed to the north of the Douay Alkaline Intrusive Complex and are part of the Taibi Group (<2685 ± 2.6 Ma; Davis et al., 2005). They are present in the lower part of drill hole DO-20-280 at approximately 290 m where a sharp contact occurs between the Douay Alkaline Intrusive Complex and green to brown conglomerates (Fig. 4f) and siltstones (Fig. 4g). The conglomerates contain clasts of rounded red feldspar-phyric arenite and gray quartzites (0.5-1 cm) in a brown to green fine-grained quartz-, feldspar-, and carbonate-dominated matrix (Fig. 4f). The main alteration assemblage consists of minerals such as quartz (60 vol%), feldspar (15 vol%), calcite (5 vol%), and chlorite (2-5 vol%), sericite (3 vol%). A sedimentary unit (one sample) contains a clast (35% of the sample) made of subangular to subrounded quartz and feldspar. The matrix (70%) consists of fine-grained quartz (30 vol%), albite (20 vol%), K-feldspar (15 vol%), and carbonate (5 vol%). Sedimentary rocks also occur at approximately 263 meters downhole in DO-21-295, where dark brown, green to grey 0.2-0.5 cm laminations can be observed in the siltstones (Fig. 4g).

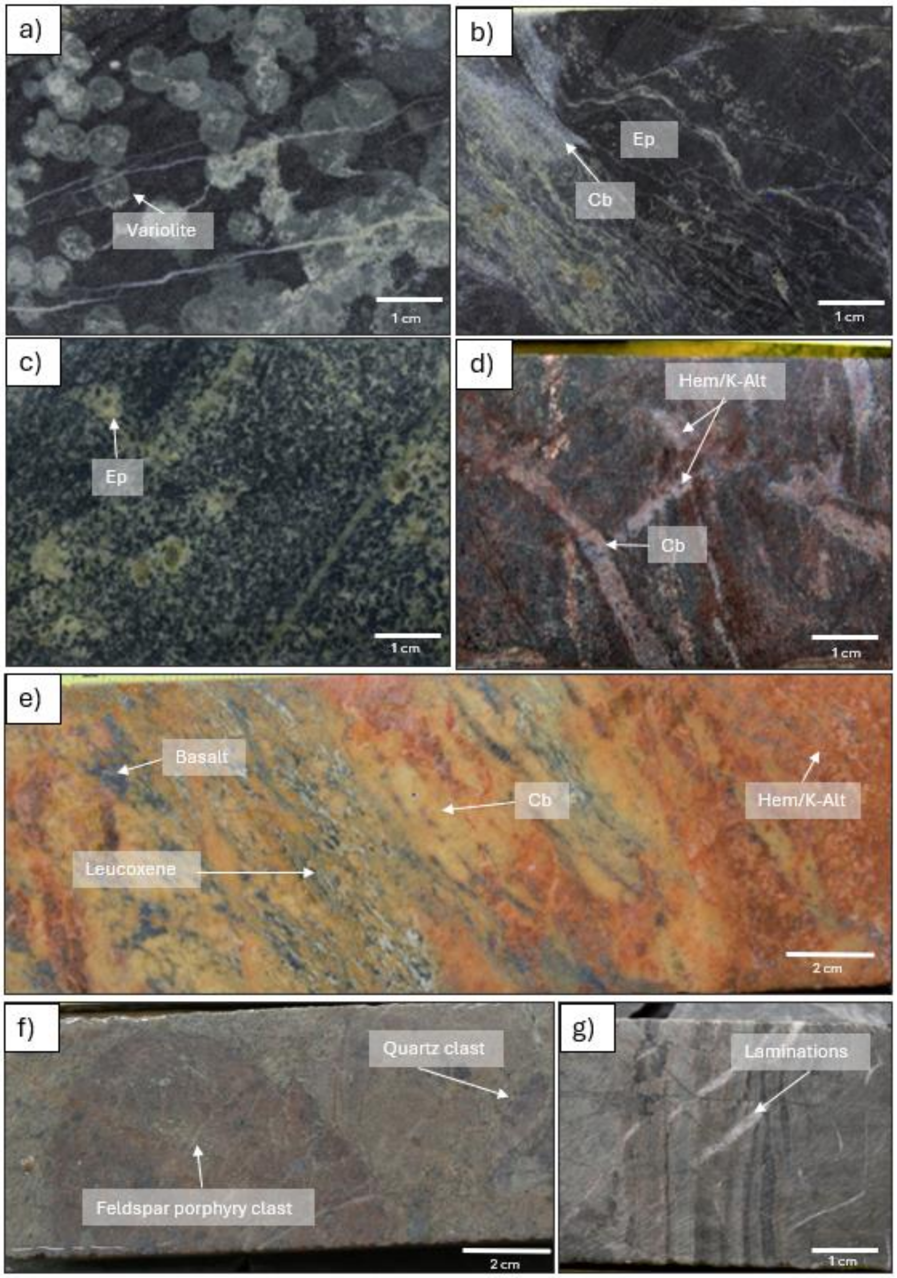

Figure 4: Mafic volcanic and sedimentary rocks located along the margins of the Douay Alkaline Intrusive Complex: **(a)** Fine-grained basalt with variolitic texture (DO-18-230 @ 52 m), **(b)** Fine-grained basalt slightly altered by green epidote and white carbonate veinlets (DO-12-97 @ 28.50 m; TW-01), **(c)** coarse-grained basalt with moderate epidote alteration (DO-11-33 @58.88 m; TW-46), **(d)** fine grained basalt with pervasive red potassic/hermitic alteration in the matrix and white carbonate veinlets (DO-12-97 @ 42 m), **(e)** orange to red, slightly foliated altered transitional zone between the basalt and Douay Alkaline Intrusive Complex (DO-12-97 @ 244.27 m; TW-16), **(f)** Conglomerate containing red feldspar porphyry and quartz clasts in a brown-green fine-grained matrix (DO-20-280 @ 289 m; TW-62), **(g)** 0.2-0.5 cm sedimentary bedding in a light green-grey siltstone (DO-21-295 @ 496 m).

4.1.3 Douay Alkaline Intrusive Complex

4.1.3.1 Least Altered Facies

The least altered portions of the intrusions occur as small intervals, ranging from 0.2 to 3 meters, primarily identified in the western part of the porphyry zone, where they crosscut the basaltic rocks of the Cartwright Hills Group. Additional small patches of minimally altered intrusions are also sporadically distributed throughout the Douay Alkaline Intrusive Complex. These intrusions range in color from white and pink to dark gray and are interpreted as the least altered due to their well-preserved magmatic textures. Specifically, they contain subhedral to euhedral, interlocking feldspar phenocrysts ranging from 1 to 3 cm in length (Fig. 4a). The dominant feldspar present is alkali feldspar (0.3–2 mm; 50–85 vol%). The matrix consists of quartz (6–12 vol%, up to 18 vol%), albite (2–10 vol%, up to 14 vol%), and carbonate (4–15 vol%). Accessory minerals include fluorite (<1–2 vol%), euhedral pyrite (1–5 vol%), and trace amounts of apatite and magnetite.

4.1.3.2 Albitized Facies

The albitized facies is observed in the southern portion of the Porphyry Zone, within proximity to the lithological contact with the sediments of the Taibi Group (Fig. 2b). The white to grey intrusive rock is referred to as the albitized facies and is mainly recognized by replacement of groundmass by minerals such as albite, minor carbonates and quartz. The rocks occasionally contain small vugs (<0.2-1cm; Fig. 4b) probably associated with the dissolution of a mineral phase. The feldspars are typically rectangular to square in shape, with white to light pink edges. The albitized intrusive facies displays massive (Fig. 4b), porphyritic (Fig. 4c), and phaneritic (Fig. 6c) textures. The albitized facies also includes aplite intrusions (Fig. 4d) that are light grey blue in color and are dominated by fine-grained feldspar and quartz that crosscut the earlier albitized phase intrusions. The main minerals are anhedral to subhedral alkali feldspar (0.5–3 mm; 40–60 vol%, locally up to

80%) that exhibit pronounced perthitic exsolution with a characteristic chessboard texture (Fig. 11c), which is more clearly revealed under cathodoluminescence, where orthoclase appears blue and albite pink (Fig. 6b). Additionally, 30-40% of the feldspar phenocrysts display a green color using cathodoluminescence, which is a result of sericitization (Fig. 6b). The matrix mainly consists of euhedral albite (3-20 vol%), quartz (5-22 vol%), carbonate (5-15 vol%), and accessory minerals such as fluorite, apatite (1-3 vol%), subhedral to euhedral pyrite (1-5 vol%), and trace magnetite.

4.1.3.3 Hematized Facies

The hematized facies is located on the western portion of the Porphyry Zone and is more associated with a minor shear zone between the Douay Alkaline Intrusive complex and the volcanic rocks of the Cartwright Hills Group. The medium pink to brick red syenite is referred to as the hematized facies and is recognized by its pink to “brick red” color (Fig. 5e). Hematized rocks contain mainly white to pink, elongated, anhedral to subhedral feldspar phenocrysts displaying perthitic texture (0.3-1.2 cm; Fig. 11d). The matrix consists of feldspar, quartz, and carbonate. The hematized facies displays massive (Fig. 5e), equigranular, and porphyritic textures (Fig. 5f & g). These facies are mostly composed (20–40 vol%, up to 71 vol%) of anhedral to subhedral alkali feldspar phenocrysts (0.5–2 mm) with irregular, rounded crystal edges (Fig. 6a & f). The matrix contains carbonate (12-30 vol%), albite (5-21 vol%), and quartz (5-22 vol%). Accessory minerals such as fluorite (1-2 vol%), apatite (<1%), and rutile (<1%) are also present. The sulfide minerals consist of subhedral to euhedral pyrite (1-5 vol%) and trace amounts of magnetite and chalcopyrite. The carbonate minerals occur as inclusions in fractured feldspar phenocrysts, at the contact between albite grains where they display replacement textures, and in the matrix. Zoning in the carbonate grains is often observed and exhibits calcite rich cores and Mg-Fe enriched rim (Fig. 11e).

4.1.3.4 Carbonatized Facies

Present in both the hematized and albitized facies, intervals of intense carbonatization corridors of 0.5-6 meters wide, are referred to as the carbonatized facies. The carbonatized facies is pink-gray-white, massive, fine-grained and tends to be overprinting and texturally destructive (Fig. 5h). The fine-grained carbonates are interlaced with subhedral to euhedral disseminated pyrite (5-30%) disseminations (Fig. 7a) and pyrite stringers (Fig. 7e). The carbonatized facies is dominated by carbonates (30-50 vol%) and anhedral alkali feldspar phenocrysts (0.5-1.5 mm; 5-20, up to 40 vol%). The edges of the feldspars are irregular, and the grains are rounded. The carbonates range in composition from Fe- to Mg-rich (Fig. 11b). The matrix consists mainly of carbonate (30-50 vol%), albite (8-25 vol%), and quartz (5-33 vol%).

4.1.3.5 Ca-rich Intrusions

The Ca-rich intrusions are observed randomly crosscutting the volcanic rocks of the Cartwright Hills Group and the Douay Alkaline Intrusive Complex. These intrusions are primarily composed of carbonate minerals, with colors ranging from white and pink to light gray. They consist of primarily calcite, along with trace amounts of quartz, fluorite, magnetite, and interstitial pyrite (Fig. 5i). The intrusions vary in size from 1 to 30 cm wide dykes or in dyke swarms that can extend over several meters (Fig. 5j). The intrusions are predominantly made up of equigranular calcite grains (0.4-0.7 mm in size, 85-90 vol%; Fig. 6h). The matrix (10-15 vol%) contains small amounts of apatite (2-3 vol%), quartz (1-3 vol%), and feldspar (1-2 vol%; Fig. 6h).

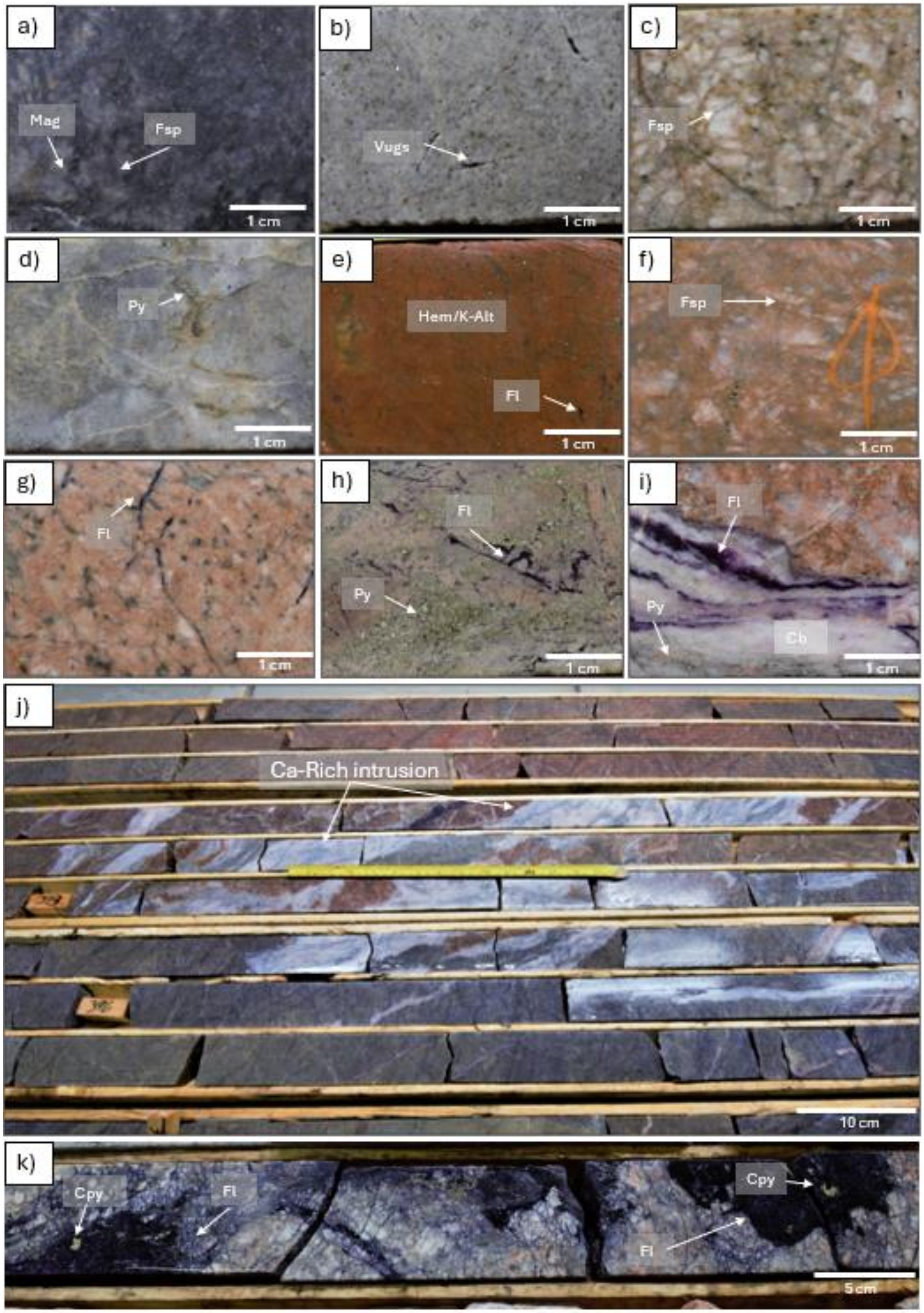
a)
Mag
Fsp
1 cm
b)
Vugs
1 cm
c)
Fsp
1 cm
d)
Py
1 cm
e)
Hem/K-Alt
Fl
1 cm
f)
Fsp
1 cm
g)
Fl
1 cm
h)
Fl
Py
1 cm
i)
Fl
Py
Cb
1 cm
j)
Ca-Rich intrusion
10 cm
k)
Cpy
Fl
Cpy
Fl
5 cm

Figure 5: Douay Alkaline Intrusive Complex facies and Ca-rich intrusion: **(a)** Dark gray least altered intrusion (DO-12-97 @ 86.12 m; TW-3A), **(b)** White-gray massive texture containing feldspar, quartz, trace fine grained pyrites, and carbonates, which are observed in the vugs (DO-20-283 @ 198.60m; TW-44), **(c)** porphyritic texture with white subhedral feldspar phenocrysts, the matrix contains fine grained feldspar, quartz, trace pyrite (DO-12-97 @ 384 m; TW-15), **(d)** Albitized facies displaying aplitic texture (DO-12-97 at 430.94m; TW-13), **(e)** Strongly hematized/potassic altered sample with carbonate, fluorite, and fine grained pyrite in the matrix representing a massive texture (DO-11-33 @ 255 m; TW-49), **(f)** Brick red Porphyritic rock with a strongly hematized matrix (DO-12-97 at 324.16 m; TW-10), **(g)** Pink porphyritic rock with a potassic altered matrix consisting of feldspar and minor quartz (DO-20-281 at 151.05m; TW-32), **(h)** Carbonatized sample showing massive texture and aligned pyrite stringer veins, with the part of the original magmatic porphyritic texture preserved represented by white feldspar phenocrysts and purple fluorite in the matrix (DO-19-256 @78 m; TW-35), **(i)** Ca-rich intrusion observed with alternating bands of purple fluorite and white calcite located in the hematized intrusive phase (DO-12-97 @ 226m; TW-05A), **(j)** Ca-Rich intrusion (white) intruding along a possible contact between the red hematized intrusion and grey albitized intrusion (DO-21-295 from 390-398m), **(k)** White albitized facies intrusion with late fluorite infilling fractures with disseminated chalcopyrite (DO-20-281 at 147.60m).

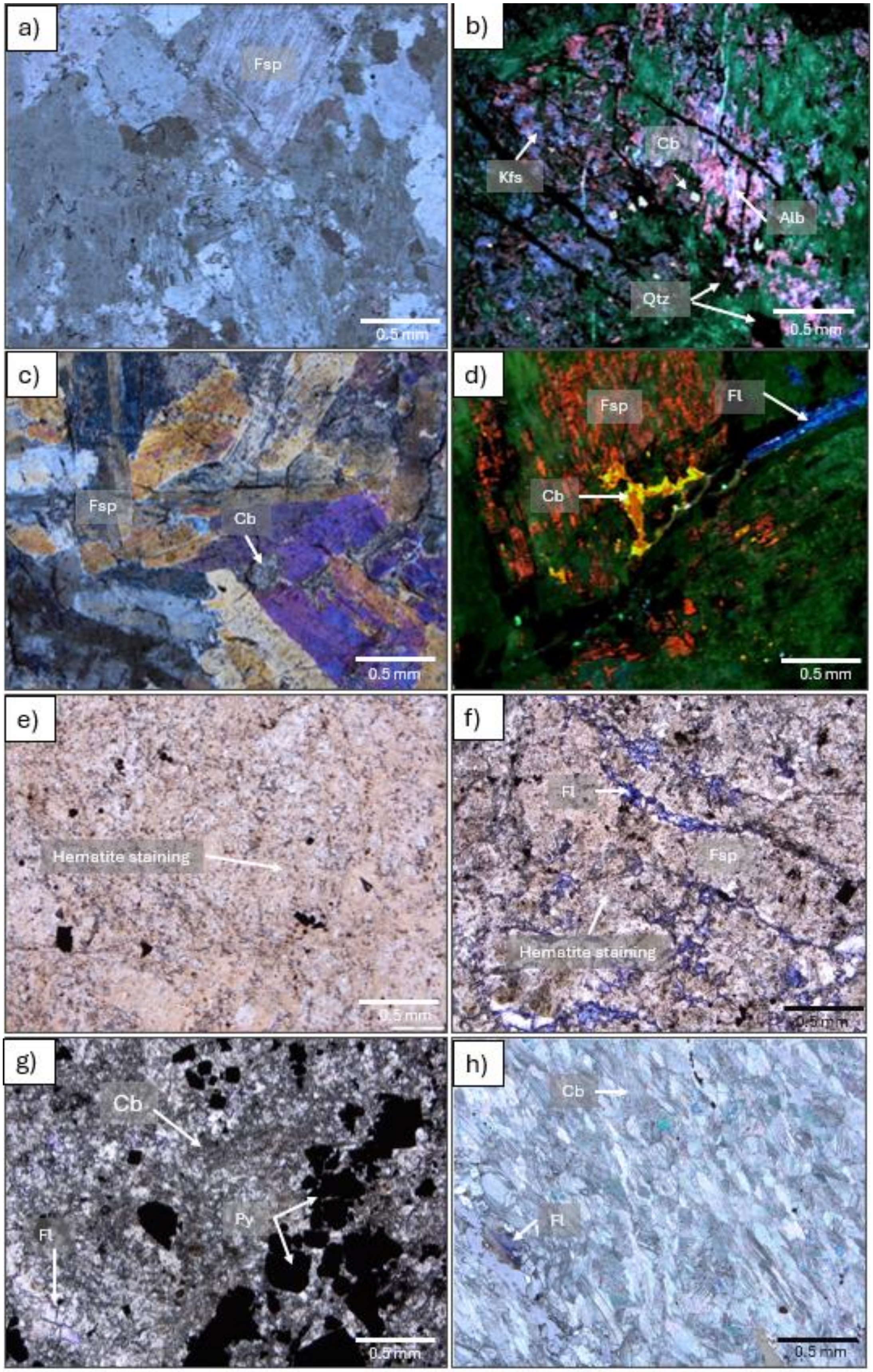
a)
Fsp
0.5 mm
b)
Kfs
Cb
Alb
Qtz
0.5 mm
c)
Fsp
Cb
0.5 mm
d)
Fsp
Fl
Cb
0.5 mm
e)
Hematite staining
0.5 mm
f)
Fl
Fsp
Hematite staining
0.5 mm
g)
Cb
Fl
Py
0.5 mm
h)
Cb
Fl
0.5 mm

Figure 6: Photomicrographs displaying the complex textures hosted in the albitized, hematized, carbonatized, ca-rich intrusions throughout the western Porphyry Zone under plane-polarized light (PPL), cross polarized light (XP), and cathodoluminescence (CL); **(a)** Photomicrograph XP showing the interlocking crystals feldspar in the albitized facies (TW-12), **(b)** CL image displaying perthite texture in the feldspar phenocrysts, specifically, K-feldspar (blue), albite (pink), patchy to pervasive sericite alteration (green), and carbonates (yellow orange) in the albitized facies (TW-15), **(c)** photomicrograph in cross polarized light (XP) displaying interlocking crystals of feldspar with minor carbonates and quartz observed in the interstitial in the albitized facies (TW-53), **(d)** cathodoluminescence (CL) image displaying feldspar phenocrysts (red) with patchy sericite alteration (green) contained in a matrix composed of quartz (black), carbonates (yellow), and minor fluorite (blue; TW-53), **(e)** photomicrograph plane-polarized light (PPL) shows massive texture in the hematized facies displaying strong red-brown hematite staining in the matrix (TW-07), **(f)** Photomicrograph in plane-polarized light (PPL) displaying a porphyritic texture with anhedral feldspar phenocrysts exhibiting weak to moderate hematitic staining, accompanied by purple fluorite, and disseminated carbonates observed in the interstitial spaces (TW-68), (**g)** Photomicrograph in plane-polarized light (PPL) showing the pervasive nature of the carbonates in the matrix within the carbonatized facies (TW-35), **(h)** photomicrograph in cross polarized light (XP) displaying equigranular texture observed in the Ca-rich intrusions (TW-05A).

4.1.4 Mineralization

Gold mineralization in the western Porphyry Zone occurs in three styles: 1) fine-grained, gold-rich disseminated pyrite, predominantly hosted in the hematized facies (Fig. 2b), which is the dominant style; 2) minor intervals of breccia; and 3) trace veins and veinlets of albite-carbonate-sulfides containing visible gold, though these are anomalous in the western Porphyry Zone (Fig. 5). Minor shear zones, such as the “Transitional Zone” (Fig. 4e), are present throughout the study area but are often barren (Fig. 4e).

The disseminated gold-rich pyrite mineralization is observed in the albitized, hematized and overprinting carbonatized facies. Gold mineralization in the albitized facies is typically associated with porphyritic intrusions, occurring in intervals ranging from 1 to 30 meters of fine grained subhedral to euhedral disseminated pyrite (2-15 vol%). Grades in the albitized facies typically range from 0.1 to 0.35 g/t. Conversely, gold mineralization hosted in the hematized facies—occurring in massive to porphyritic “brick red” to pink intrusions—is generally low grade (0.1 to 1.5 g/t) and extends over intervals of 10 to 150 meters. This type of mineralization is frequently associated with fine- to medium-grained disseminated pyrite (2–20 vol%) and minor chalcopyrite (1–3 vol%; Fig. 5k

& 7c). Anomalous higher-grade (5 to 8.9 g/t gold) intervals (0.5-to-3-meter) are associated with carbonatized facies, which is texturally destructive and overprints the hematized facies consisting of aligned pyrite stringer (20-35 vol%) veinlets.

Breccias are observed throughout the Douay Alkaline Intrusive Complex, with intervals ranging from 0.2-4 meters with gold grades between 0.2 to 3 g/t gold. The breccias can be monomict or polymictic, with the matrix consisting of fine to medium grained carbonate, grey quartz, and occasional purple fluorite. The matrix contains fine to medium grained disseminated pyrite (2-10 vol%) and minor disseminated chalcopyrite (2-4 vol%), which is often associated with purple fluorite in the matrix (Fig. 5k).

Three main mineralized vein types were observed in the western porphyry zone and classified as V_1, V_2, and V_3 based on relative chronology, mineralogy, and morphology (Table 1). V_1 veins mainly consist of albite, ankerite, and trace quartz (Fig. 8a, b, c). Also, V_1 veins contain anhedral and euhedral pyrite, chalcopyrite, specularite, magnetite, and trace of free gold (Fig. 8a, b, c). V_2 veins are characterized by 0.2-0.8 mm width, and are mainly composed of calcite, albite, quartz, fluorite, and trace apatite (Fig. 8d). V_3 veins consist of 0.3-7 mm width barite-anhydrite veins, which crosscuts all vein types (Fig.8e).

The most uncommon style of mineralization is the polymetallic veins (V_1), mainly composed of albite, ankerite, and trace quartz. The V1 veins contain sulfides such as pyrite with minor chalcopyrite, specularite (Fig. 8b & c), molybdenite, and sometimes visible gold (Fig. 8a). The extensional 1-3 cm veins are rare and contain the highest gold values in the western porphyry zone grading 334 g/t gold (DO-21-297 depth: 56-57m; Maple Gold Mines Ltd, 2021).

Detailed petrographic analysis (Supplementary Information #S1C) was performed on the mineralized samples in each intrusive facies. Gold is almost systematically associated with pyrite.

The pyrite grains observed in the matrix of the hematized and albitized facies, tend to be large (0.2-2 mm) subhedral to euhedral grains that display inclusion-rich cores and inclusion-poor rims (Fig. 7a). In the carbonatized facies, the pyrite grains are anhedral to subhedral, large (0.2-3.5mm), display inclusion-rich cores and inclusion-poor rims (20-40 µm), and irregular grain boundaries (Fig. 7b, c, e, & f). Additionally, some of the subhedral pyrites in the carbonatized phase tend to have minor inclusions and appear recrystallized (Fig. 7b). Most inclusions are small (~10-25 µm) and correspond to silicate, carbonate, as well as minor barite, galena, sphalerite, chalcopyrite, and occasionally gold inclusions.

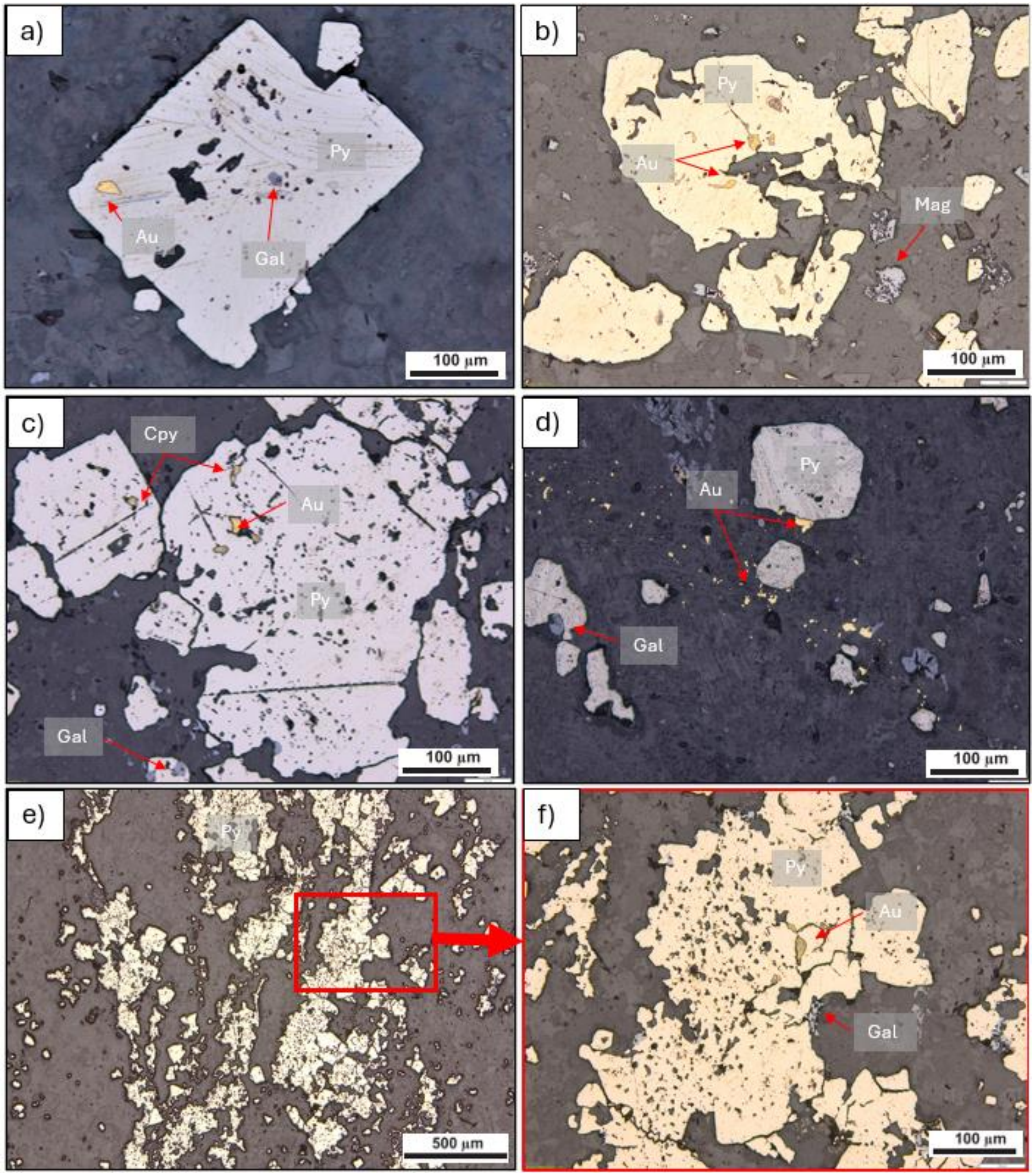

Figure 7: Reflected light photomicrographs displaying the complex textures displayed in the pyrite grains associated with mineralization in the western porphyry zone; **(a)** pyrite grain with an inclusion rich core consisting of galena and Au inclusion observed in the rim located in the albitized facies (DO-20-283 at 198.6m; TW-44), **(b)** elongate clusters of recrystallized pyrite grains with Au inclusions in the carbonatized facies (DO-21-295 at 57.7m; TW-72), **(c)** subhedral to anhedral pyrite grains with inclusions of chalcopyrite and galena in the carbonatized facies (DO-19-256 at 80.4m; TW-63), **(d)** subhedral pyrites inclusion poor with Au grains along the crystal and free gold disseminated in carbonate veinlet observed in the carbonatized facies (DO-19-256 @ 80.4m; TW-63), **(e)** elongate clusters of pyrites ('stringers') in the carbonatized facies (DO-21-295 @ 57.7m; TW-72), **(f)** The red box is a zoomed to 100 µm of image (e) representing the inclusion rich cores, inclusion poor rims, and fractures in pyrite crystals with Au (DO-21-295 at 57.7m; TW-72).

Table 1: Summary of veins: Mineral abbreviations: Alb = albite, Au = native gold, cpy = chalcopyrite, fl = fluorite, hem = hematite, ksp = K-feldspar, mol = molybdenite, spc = Specularite, py = pyrite, qtz = quartz, any= anhydrite, ba = barite

Feature	**V_1**	**V_2**	**V_3**
Width	<0.2-2.5cm	0.5-3 cm	0.1- 0.3 cm
Mineralogy	alb + qtz + cc +ank	alb + cc ± fl, ap, qtz	any + ba
Mineralization	py, spec, mol, cpy, ± Au	py	

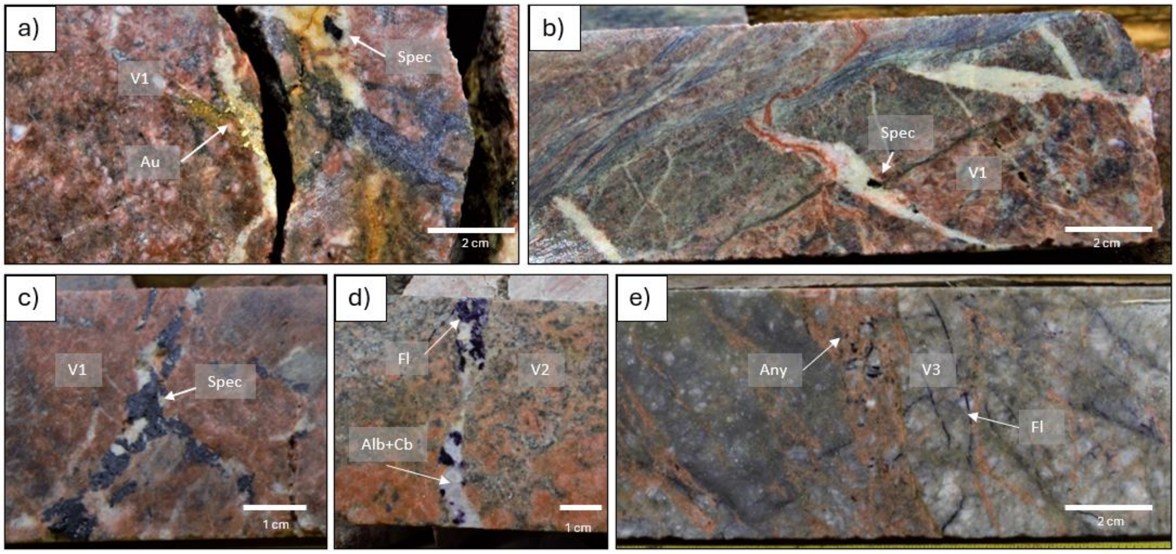

Figure 8: **(a)** V_1 Albite-quartz-carbonate veins at a high angle to core axis crosscutting a syenitic intrusion (hematized facies; DO-21-295 @ 57.5m), **(b)** extensional albite-carbonate V_1 veins with disseminated hematite crosscutting the hematized facies and carbonatized facies rock (DO-21-295 @ 56.52m) ; **(c)** V_1-veins Albite-carbonate veins with dark grey specularite (DO-21-295@ 77m) at a high angle to core axis crosscutting a syenite intrusion (hematized facies), **(d)** V_2 veins at high angle to core axis composed of albite-carbonate-fluorite (DO-12-97 @ 261.65 m; TW-05), **(e)** V_3 veins tend to be light pink composed of sulfate minerals such as barite and anhydrite (DO-12-97 @ 362.71 m at 362.71m).

4.2 Geochemistry

4.2.1 Whole Rock Geochemistry

The 42 whole rock analyses are classified using field observations, and the categories are: volcanic rocks (n=8), as well as Douay Alkaline Intrusive Complex least altered (n=4), albitized (n=16), hematized (n=10), carbonatized (n=4), and the Ca-rich intrusions. The whole rock analyses were compared to historical data (SIGEOM, n=52) and outcrop samples (n=5) from Mathieu et al. (2022) and was first plotted on a Total Alkali Silica (TAS) diagram (Fig. 9a).

Despite being intended for unaltered rocks, the TAS diagram (Fig. 9a) was used due to the lack of trace element information available in the historical data (SIGEOM). This diagram was utilized to compare the historical data set to the Douay Alkaline Intrusive Complex samples of this study. The historical data displayed a trend from foidolite to syenite field, similar to the whole rock analyses of this study.

The whole rock analyses of the Douay Alkaline Intrusive Complex plot in the syenite and monzonite fields, with the Ca-rich intrusions phase plotting in the foidolite and foid-monzodiorite fields. The four least altered samples plot within the syenite field. Furthermore, the Winchester and Floyd diagram (Fig. 9b) was used to verify the results of the TAS diagram due to the extent of the alteration present in the Douay Alkaline Intrusive Complex. The rocks plotted predominantly in the trachyte (syenite) and trachyte-andesite (syenite to monzonite) fields, with all four of the least altered facies samples plotting in the trachyte field, confirming the results of the TAS diagram.

On the REE and multi element diagrams (Fig. 9c & d; Hoffmann, 1988), the main intrusive phases of the Douay Alkaline Intrusive Complex display similar profiles. The REE profiles are enriched in LREE and depleted in the HREE, with increasing fractionation from the carbonatized facies, with $(La/Yb)_N = 15$, the least altered facies with $(La/Yb)_N = 38.6$ (median value), the hematized facies with $(La/Yb)_N = 44.9$, and the albitized facies with $(La/Yb)_N = 46.8$ (median value). The studied albitized, hematized, and carbonatized facies display negative Nb, Ta, Zr-Hf, and Ti anomalies, with no Eu anomaly on the multielement diagram (Fig. 9c).

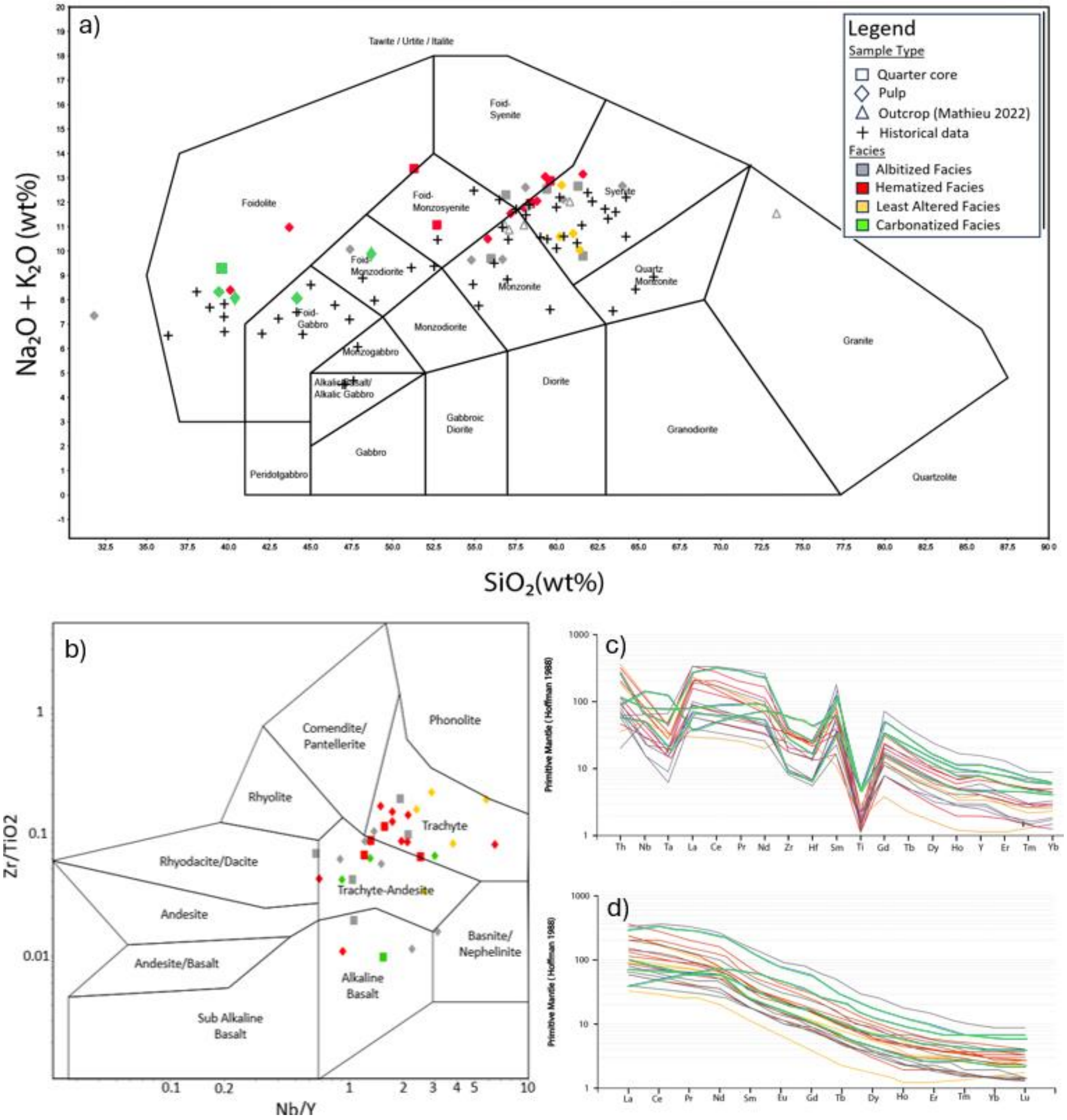

Figure 9: Chemical composition of 42 rock samples from the western porphyry zone, 45 samples from SIGEOM, and 4 samples from Mathieu (2022) are displayed on **(a)** the Total Alkali Silicate (TAS) binary diagram (Middlemost, 1994) **(b)** Winchester and Floyd (1977), **(c)** a primitive mantle-normalized REE plot (Hoffman, 1988), **(d)** a primitive mantle-normalized multi-element diagram modified from (Pearce, 2008).

Table 2: Table presenting average whole-rock geochemical data for volcanic rocks and for distinct facies of the Douay Alkaline Intrusive Complex, including the least altered, hematized, and carbonatized.

	Volcanic Rock (n=8)	**Least Altered (n=5)**	**Albitized (n=12)**	**Hematized (n=13)**	**Carbonatized (n=4)**
SiO_2 (wt%)	41.1	58.02	55.23	55.19	42.03
Al_2O_3	12.05	16.34	15.69	15.9	12.54
$Fe_2O_{3(T)}$	9.23	4.97	4.08	3.88	7.56
CaO	13.74	4.71	5.23	5.13	10.33
MgO	5.97	1.71	1.08	1.12	2.82
Na_2O	3.92	7.34	6.15	4.66	2.79
K_2O	2.34	3.48	4.71	6.99	6.11
Cr_2O_3	0.04	0.01	0.006	0.006	0.01
TiO_2	0.67	0.37	0.36	0.36	0.7
MnO	0.23	0.11	0.09	0.1	0.22
P_2O_5	0.77	0.27	0.2	0.48	0.87
SrO	0.16	0.07	0.13	0.04	0.06
BaO	0.14	0.08	0.09	0.06	0.11
Total	100.02	100.76	98.86	99.12	98.3
LOI	9.71	3.3	5.86	5.22	12.18
Ba (ppm)	1124.94	755.2	793.08	534.42	956.25
Ce	189.91	177.2	138.76	226.48	182.38
Cr	295	72	29.17	31.54	70
Cs	5.48	1.88	0.73	1.24	1.5
Dy	8.19	3.13	3.21	5.06	7.06
Er	3.31	1.36	1.25	1.97	2.63
Eu	5.73	2.58	2.66	4.18	5.85

Ga	19.95	32.72	23.22	26.7	22.5
Gd	15.31	6.35	6.81	10.7	15.3
Ge	<5	<5	<5	<5	<5
Hf	3.89	7.4	3.72	5.35	5.48
Ho	1.38	0.53	0.52	0.81	1.13
La	75.2	83.58	61.78	95.98	64.88
Lu	0.36	0.21	0.13	0.21	0.29
Nb	26.26	46.84	22.39	34.91	47.48
Nd	110.61	74.92	67.61	107.94	116.43
Pr	25.52	20.79	17.22	27.65	26.29
Rb	95.1	112.44	121.96	181.24	157.8
Sm	22.3	11.26	11.25	17.82	24.43
Sn	1.14	1	1	1	1
Sr	1281.51	615.8	1132.42	355.92	547.75
Ta	1.28	1.16	0.68	0.98	2.13
Tb	1.75	0.67	0.73	1.13	1.62
Th	8.43	15.59	7.77	13.74	9.34
Tm	0.42	0.19	0.15	0.25	0.33
U	2.2	4.74	2.65	3.68	2.5
V	244.5	142.4	106.17	128.38	247.5
W	1.63	11.8	26.5	32.54	24.25
Y	36.38	13.96	14.77	23.12	29.85
Yb	2.49	1.27	0.93	1.49	1.91
Au	0.004	1.46	0.3	0.5	1.59
Zr	225.13	376.6	195.17	285.31	306.75
Ag	<0.005	3.05	0.94	0.8	0.6
Cd	<0.5	<0.5	0.5	<0.5	0.5
Co	40.5	12	11.42	9.23	21

Cu	113.25	411.2	55.42	177.15	68.5
Li	97.5	30	24	22.5	50
Mo	7.17	1.2	3.11	31.57	1.25
Ni	162.88	36	25.1	18.4	39.75
Pb	10.5	8	11.15	12.5	12.25
Sc	17.5	7.2	4	4.08	12
Zn	104.63	68.4	61.33	58.69	94
As	10.31	2.02	3.67	2.67	6
Bi	0.1	0.33	0.55	0.78	0.14
Hg	<0.005	0.04	0.007	0.01	0.01
In	0.03	0.02	0.01	0.02	0.03
Re	0.001	0.002	0.002	0.028	0.002
Sb	0.5	1.4	0.47	0.65	0.44
Se	0.54	0.27	0.84	0.67	0.53
Te	0.04	0.58	0.28	0.26	0.11
Tl	0.24	0.12	0.03	0.07	0.04
C	2.41	0.76	1.55	1.45	3.61
S	0.41	0.64	1.52	0.7	0.67
H_2O^+	1.88	0.33	0.28	0.26	0.38
Cl	67.5	77.5	148.33	91.82	76.67
F	1656.25	2188	3078.5	4637.69	1900

4.2.2 Mass Balance

In order to assess the hydrothermal alteration associated with the gold mineralization, detailed petrographic and geochemical analyses were conducted to try and identify the mineral and alteration assemblages within the intrusive rocks of the Douay Alkaline Intrusive Complex.

The Trépanier method utilizes artificial neural networks (ANN) to forecast a precursor for volcanic rocks that have been altered by hydrothermal processes (Trépanier et al., 2016). The goal is to accurately determine the concentrations of the main components in the unaltered precursor rock, specifically SiO_2, FeO_T, MgO, CaO, Na_2O, and K_2O, using typical immobile elements such as Zr, TiO_2, Al_2O_3, Y, Nb, Th, and Cr (Trépanier et al., 2016). Mass changes returned by the method of are considered negligible when they are between -1 and +1 g for 100 g of precursor for most elements and between -10 and +10 g for silica (Trépanier et al., 2016). Whole rock analysis reveals two predominant alteration types: sodic and potassic alteration, consistent with petrographic observations. These alteration types are generally not observed simultaneously, except in samples exhibiting significant positive gains in both Na and K. Additionally, for the albitized, hematized, and carbonatized facies the mass change data for K_2O and Na_2O were determined, with a focus on the intrusive phases. The results revealed a negative correlation between K_2O and Na_2O (Fig. 10), further supporting that the sodic and potassic alterations typically occurred as two separate alteration events.

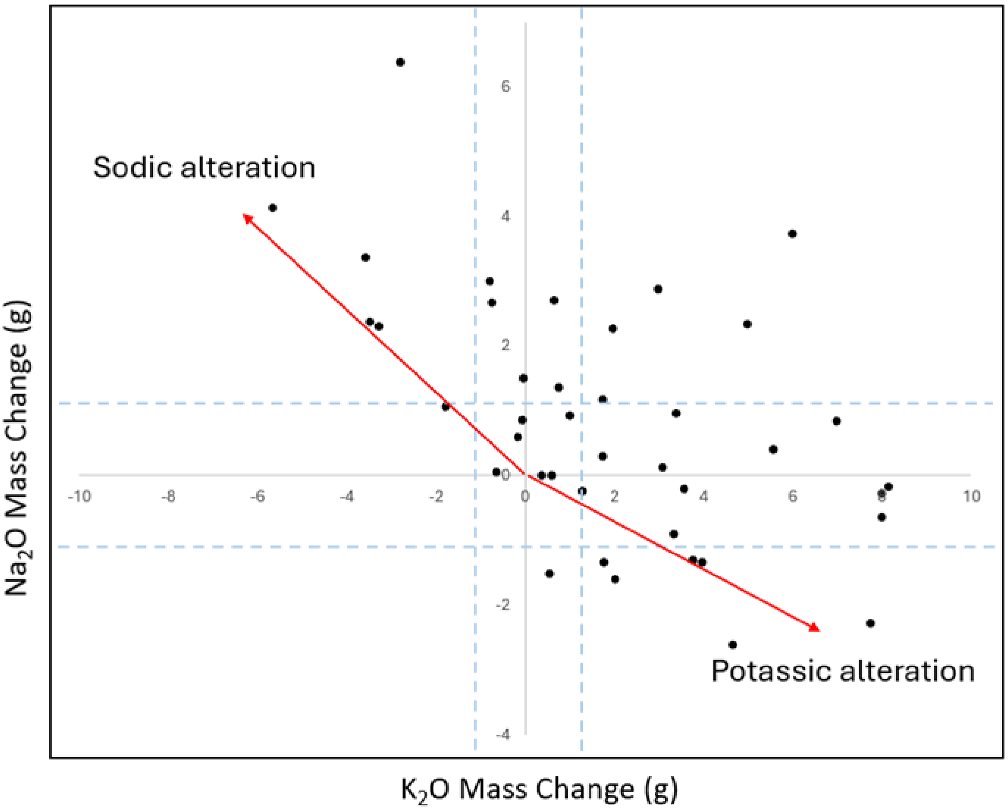

Figure 10: The results for mass changes between the Na_2O vs K_2O. The origin of the diagram represents the calculated precursor using the method of Trépanier et al. (2016). Note that K- and Na- gains are negatively correlated.

4.2.3 Trace element signature of mineralization

The whole rock geochemistry of mineralized samples (n=17; Supplementary Information #S1D) with gold concentrations greater than 300 ppb reveals an Au/Ag ratio of 1.5. Pearson correlation analysis shows that Ag, W, Hg, Te, and Sb display moderate to positive correlations with Au, with correlation coefficients ranging from 0.3 to 0.5. This correlation pattern emphasizes the polymetallic signature of the mineralizing fluids.

4.3 Mineral Chemistry

4.3.1 Scanning Electron Microprobe

The general chemistry of the feldspars is primarily orthoclase to albite in all intrusive facies, although two samples from least altered intrusive facies plotted in the anorthosite field (Fig. 11a). The alkali feldspar phenocrysts display mosaic perthitic texture presenting albite replacement with possible relics of the original feldspar crystal (Fig. 11c & d). The shades of gray represent the approximate chemical composition of the feldspar. Orthoclase (microcline) feldspar is white to pale gray (10 -14 wt% K_2O) and albite feldspar is dark gray to black (9-14 wt% Na_2O) and match with the EDS analyses (n=1279).

From the EDS analysis (n=879), the carbonate minerals in each facies range in composition from calcite (Ca-) to dolomite (Mg-) to ankerite (Fe-; Fig. 11b). The least altered facies contain mainly Ca- to Mg-rich carbonates, whereas the albitized, hematized, and carbonatized facies is mainly composed of Mg- to Fe- rich carbonate minerals. Carbonate minerals are present as inclusions in fractured feldspar phenocrysts along the edges of albite replacement textures, matrix, and veins (Fig. 11d & e). The calcite appears to be associated with veins containing fluorite or associated with Ca-rich intrusions (TW-05 & TW-05A), which tend to be associated with trace amounts of Sr. The calcite composition dominates the center of the mineral grain, whereas the outer edges of the grain are compositionally Mg- and Fe- carbonate (Fig. 11e). The ternary diagram for carbonates illustrates that the least altered samples have an abundance of dolomite and hematized samples are dominated by ankerite (Fig. 11).

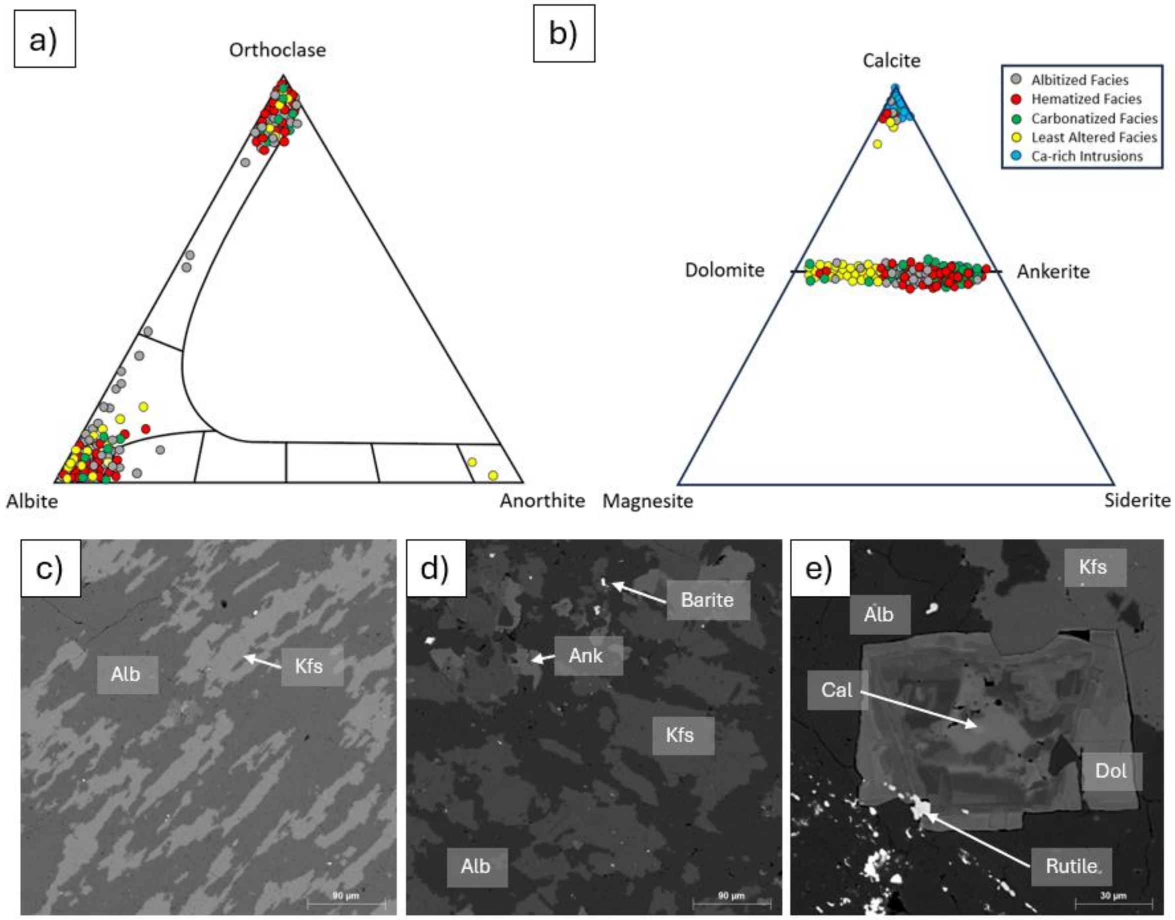

Figure 11: (a) Ternary diagrams displaying feldspars from EDS analysis, **(b)** Ternary diagram of carbonate chemistry from EDS analysis, **(c)** SEM photo showing the perthitic texture between the K-feldspar (light grey) and albite (dark-grey/black) sample number TW-23_C5 (albitized facies) **(d)** SEM photo showing the perthitic texture between the K-feldspar (light grey) and albite (dark-grey/black), sample number TW-07_17P (hematized facies); **(e)** SEM images of carbonate crystal showing possible zoning/alteration with a Ca-rich center and Mg-rich outer rim TW_09_H6 (hematized facies).

4.3.2 Pyrite Chemistry

Pyrite is common in hydrothermal-magmatic systems and records key fluid parameters such as temperature, pH, and redox conditions as it precipitates out of the fluid (Deditius et al., 2014). It also can incorporate significant trace elements and metals as inclusions or within the crystal structure (Deditius et al., 2011; Large et al., 2009; Roberts, 1982). To understand the element and metal distribution in the pyrite grains, quantitative LA-ICP-MS analyses were performed on pyrite grains from each intrusive facies, focusing on the core and rims of the pyrite grains.

Median values were then calculated for each lithological unit to compare the core and rim of the analyzed pyrite (Supplementary Information #S4C). The median values were plotted on box and whisker plots (Fig. 14a) and multielement diagrams (Fig. 14b) to define chemical differences between the core, rim, and whole grain analyses. Furthermore, box and whisker plots were generated for pyrite associated with each intrusive facies described below (Fig. 15).

The core of the pyrite grains in the albitized facies, hematized facies, and carbonatized facies show very similar chemistry. The albitized intrusive facies display modest enrichments of Pb, Te, Co, and Ag, in the cores of the pyrite grains (Fig. 15a). Whereas the hematized facies is slightly more enriched in Co, Ba, As. The cores of the pyrites in the carbonatized facies are 'stringer pyrites,' which are relatively more enriched in Ni, Cu, Zn, Cd, Mo, and As (Fig. 15b & c). Gold appears slightly more enriched in the cores (Fig. 13a) of the albitized and hematized facies than in the carbonatized facies (Fig. 15; Supplementary Information #S4A).

The rims of the pyrite grains display minor differences from the core analysis. In the albitized and hematized facies, similar chemistry is observed and on average show slightly higher concentrations of Co, Ag, Ba, Bi, and Pb (Fig. 15a & b). The carbonatized facies rims are enriched in Cu, Zn, As, Mo, and Pb (Fig. 15c). Minor gold inclusions were observed in the rims of the pyrite of the carbonatized facies (Fig. 13c). The gold inclusions are either isolated (Fig. 9a) in pyrite or associated with fractures (Fig. 9b & f). Other inclusions such as chalcopyrite, galena, and sphalerite in all facies may be controlling the distribution of elements such as Cu, Zn, and Pb.

The single integrations used for texturally homogeneous pyrite grains display different chemistry for albitized, hematized, and carbonatized facies. The albitized and hematized facies show similar chemistry, with enrichments in elements such as Te, Bi, and W (Fig. 15 a & b). The carbonatized facies, when compared to the albitized and hematized facies, have higher concentrations of Co, Zn, In, and As (Fig. 15b & c). Generally, the results display minor differences and plot in a similar pattern between each of the intrusive phases (Fig. 14b, c, & d).

Using binary diagrams, the albitized, hematized, and carbonatized facies, revealed correlations ranging from weak (r=0.0-0.4), moderate (r=0.4-0.7), to strong (r=0.7-1.0). The albitized facies displayed weak correlations between As-Au (r=0.18, Fig. 14b), and Co-Ni (r=0.03, Fig. 14f), moderate correlation between Cu-Au (r=0.53, Fig. 14e), and strong correlations between Ag-Au (r=0.80, Fig. 14a), Ag-Pb (r=0.85, Fig. 16c), Te-Au (r=0.77, Fig. 14d), Bi-Pb (r=0.9, Fig. 14g), and Te-Bi (r=0.75, Fig. 14h). The hematized facies displayed similar correlations observed in the albitized facies with the same elements. The hematized facies only displayed weak correlations between As-Au (r=0.37, Fig. 14b) and Cu-Au (r=0.39, Fig. 14e), with moderate correlations between Co-Ni (r=0.59, Fig. 16f) and Te-Bi (r=0.59, Fig. 14h), and strong correlations between Ag-Au (r=0.71, Fig. 14a), Ag-Pb (r=0.75, Fig. 14c), Te-Au (r=0.78, Fig. 14d), and Bi-Pb (r=0.91, Fig. 14g). The carbonatized facies displayed minor differences when comparing the correlation coefficients to the albitized and hematized facies. The carbonatized facies displayed weak correlations between As-Au (r=0.11, Fig. 14b), Cu-Au (r=0.21, Fig. 14e), and Co-Ni (r=0.05, Fig. 14f). Moderate correlations were observed between Ag-Pb (r=0.41, Fig. 14c) and Te-Au (r=0.66, Fig. 14d). The strongest correlations in the carbonatized facies were observed between Ag-Au (r=0.72, Fig. 14a), Bi-Pb (r=0.74, Fig. 14g), and Te-Bi (r=0.74, Fig. 14h). Overall, there is a moderate to strong correlation between Au, Te, Ag, and Bi, in the albitized, hematized, and carbonatized facies, with a weaker correlation with As and Cu.

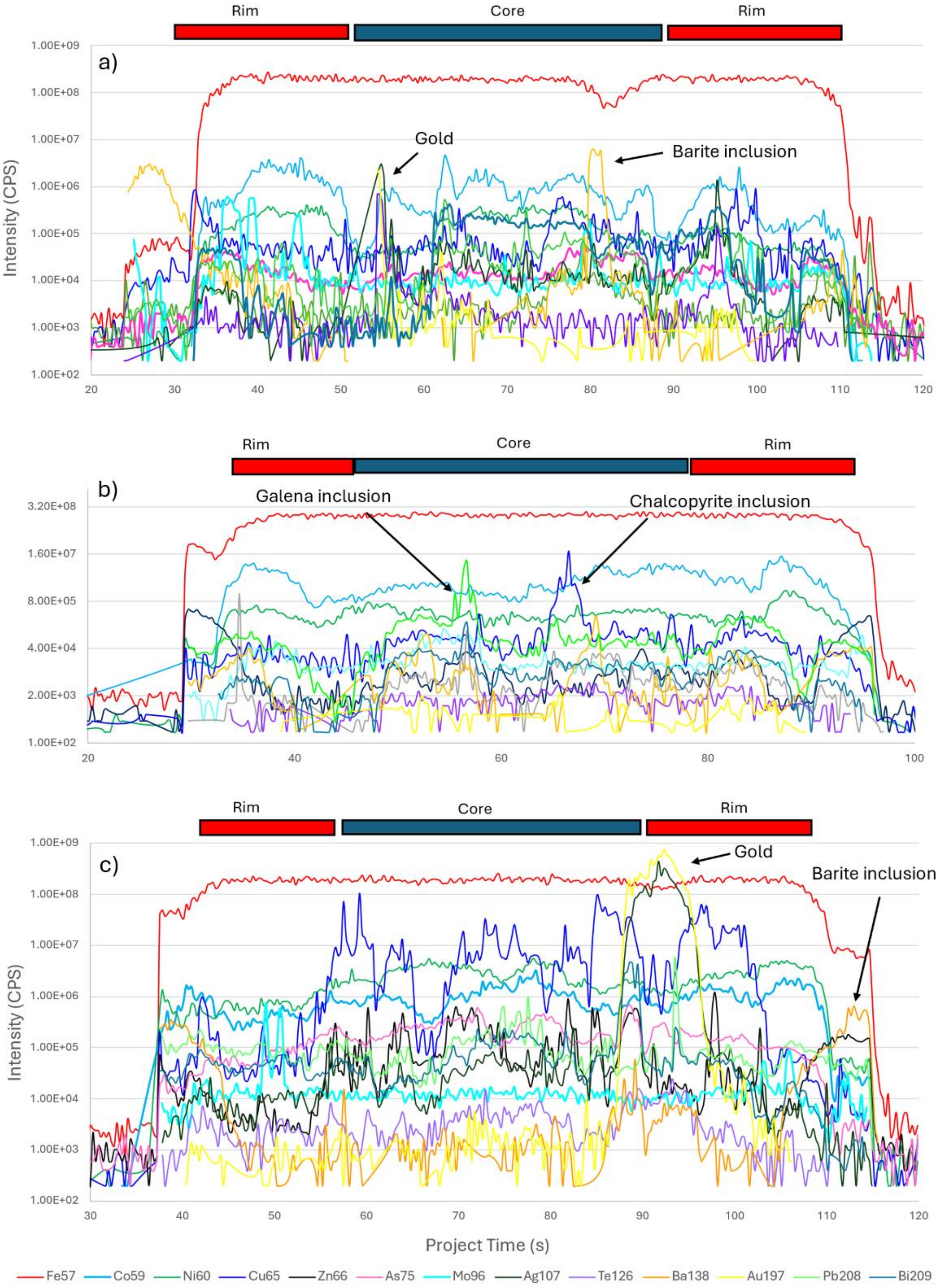

Figure 12: Time-resolved profiles in pyrite grains from the LA-ICP-MS analysis showing the distribution of ^{57}Fe, ^{59}Co, ^{60}Ni, ^{65}Cu, ^{66}Zn, ^{75}As, ^{96}Mo, ^{107}Ag, ^{126}Te, ^{138}Ba, ^{197}Au, ^{208}Pb, and ^{209}Bi: **(a)** The integration (TW-70_1; Hematized facies) display gold, silver and barium enrichment in the core of the pyrite, **(b)** The integration (TW-35_07; carbonatized facies) shows galena, and chalcopyrite inclusions within the core of the pyrite, **(c)** The integration (TW-63_2A_1; carbonatized facies) reveals a copper rich core with gold and silver rich inclusions in the rim of the pyrite and peaks of barite in the rim of the pyrite.

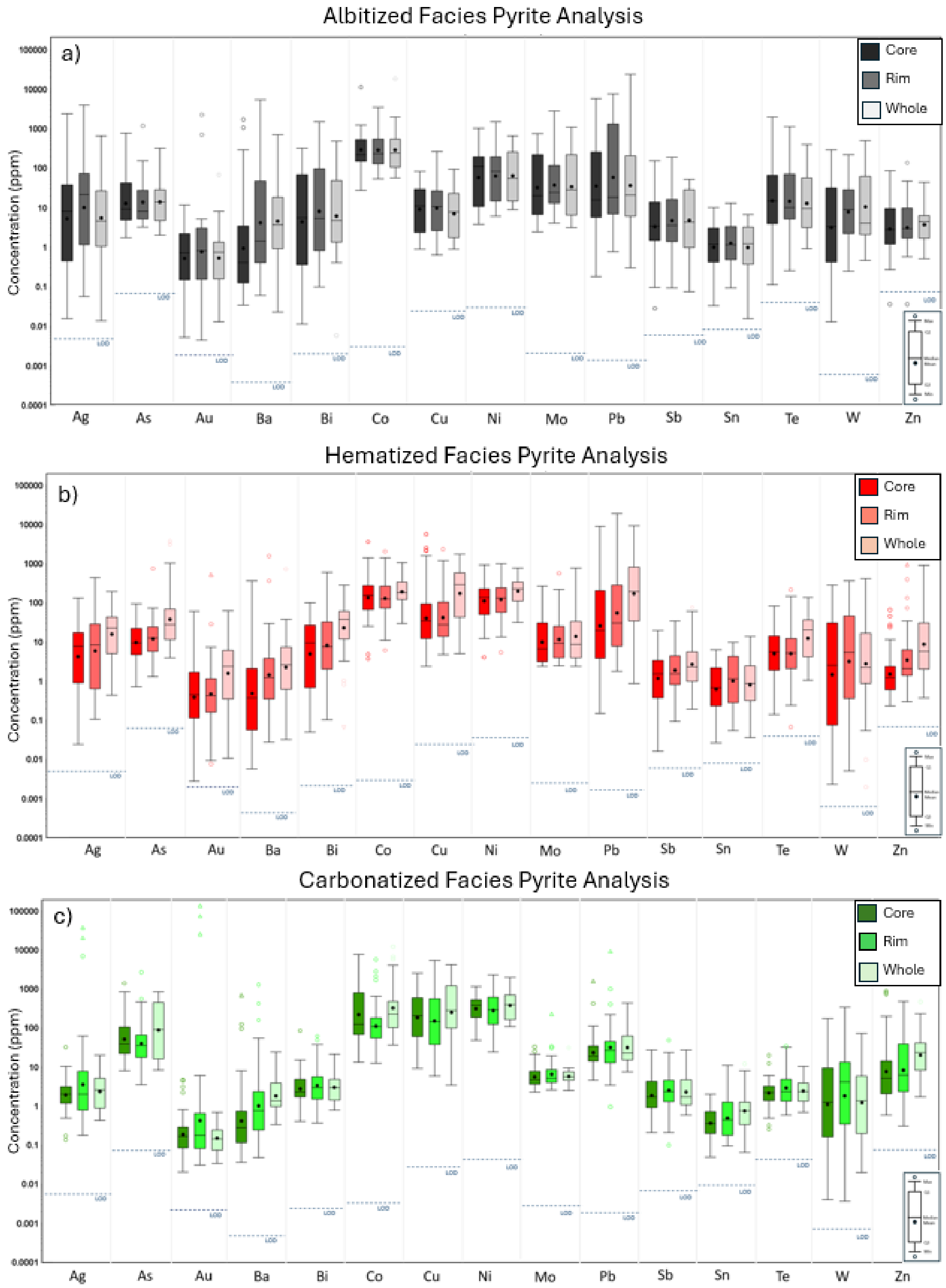

Figure 13: Pyrite chemical composition of the albitized, hematized, and carbonatized facies from the Douay Alkaline Intrusive Complex. **(a)** Box plot displaying core (n=26), rim (n=26), and whole (n=22) analysis in the albitized facies, **(b)** Box plot displaying core (n=55), rim (n=51), and whole (n=44) analysis in the hematized facies, **(c)** Box plot displaying core (n=55), rim (n=53), and whole (n=28) analysis in the carbonatized facies. LOD: Limit of detection.

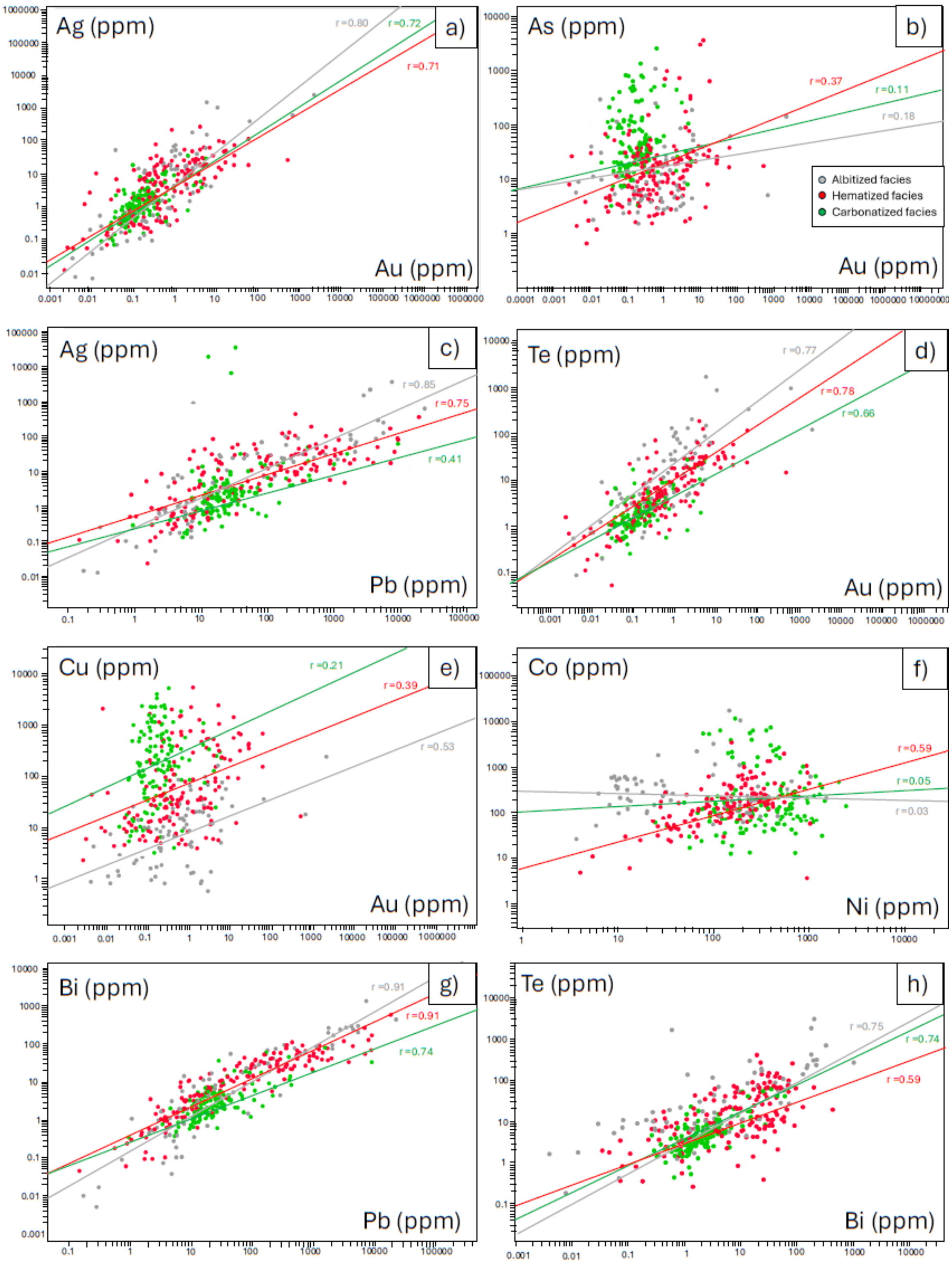

Figure 14: Binary diagrams comparing the chemistry of the pyrite grains hosted in the albitized (gray), hematized (red), and carbonatized (green) facies with correlation coefficients ranging from weak (r=0.0-0.4), moderate (r=0.4-0.7), to strong (r=0.7-1.0); **(a)** Ag-Au, **(b)** As-Au, **(c)** Ag-Pb, **(d)** Te-Au, **(e)** Cu-Au, **(f)** Co-Ni, **(g)** Bi-Pb, **(h)** Te-Bi.

CHAPTER 5: DISCUSSION

5.1 Emplacement and Hydrothermal Alteration of the Douay Alkaline Intrusive Complex

The Douay Alkaline Intrusive Complex was emplaced within close proximity to the Casa Berardi Tectonic Zone (CBTZ), which straddles the lithological boundary between the Taibi Group to the north and the Cartwright Hills Group to the south (Fig. 1). The Douay Alkaline Intrusive Complex is composed of a suite of magmatic intrusions, with compositions varying from monzonite to quartz syenites (Fig. 9a). Alkali magmas are derived from low degrees of partial melting of the mantle (Fitton and Upton, 1987) are often enriched in volatile elements (i.e. fluorine and chlorine), and incompatible elements.

The alkaline origin of the magma is supported by its geochemistry, which shows significant LREE-HREE fractionation, no Eu anomaly, and negative Nb, Ta, Zr-Hf, and Ti anomalies on a multielement diagram (Fig. 9c). The absence of an Eu anomaly has frequently been found in Archean alkaline intrusions; this is typically explained by the oxidizing conditions under which the intrusions crystallize (Cullers and Graf, 1984a; Cullers and Graf, 1984b; Rowins et al., 1993; Fayol and Jébrak, 2017). This geochemical signature is similar to other Archean alkaline intrusions located in the northern Abitibi, such as the O'Brien stock located at Lac Bachelor and Boyvinet stock (Côté-Lavoie, 2016, Fayol and Jébrak, 2017).

Fluorite is a common accessory mineral in the Douay Alkaline Intrusive Complex and has also been documented in the O'Brien intrusive of the Lac Bachelor Au mine (Fayol and Jébrak, 2017). During the crystallization of alkaline magmas, the fluorine content increases in the melt, as hydrous phenocrysts develop (Müller et al., 2001). This process allows fluorine-enriched magmatic fluids that are generated by volatile-rich alkaline magmas, to seep and alter into the surrounding host rocks

(Müller et al., 2001). The increase in fluorine content occurs in the later stages of the magmatic-hydrothermal system and is probably not related to any overprinting or remobilization by late metamorphic fluids in the western Porphyry zone. According to Dingwell and Scarfe (1985), fluorine decreases the liquidus-solidus temperature, which lengthens the magmatic process. Therefore, suggesting a long-lived magmatic-hydrothermal system.

The Douay Alkaline Intrusive Complex is an extensively metasomatized multiphase alkaline complex. Specific magmatic phases/protoliths were difficult to identify due to the large volume of fluids released during crystallization, which lead to widespread intense magmatic-hydrothermal alteration. In the western portion of the Porphyry Zone three main alteration facies are documented: 1. Albitized facies, 2. Hematized facies, and 3. Carbonatized facies.

The magmatic-hydrothermal alteration is widespread around the Douay Alkaline Intrusive Complex. The lithological contact between the volcanic and sedimentary rocks, are exploited by the intrusions, and exhibit variable hydrothermal alteration intensities, which depend on the proximity to the Douay Alkaline Intrusive Complex (Fig. 5). The volcanic rocks distal to the Douay Alkaline Intrusive Complex are characterized by moderate carbonatization and chloritization, which could have resulted from either greenschist metamorphism, seawater alteration, or propylic alteration related to the intrusion complex. The basalts proximal to the Douay Alkaline Intrusive Complex are characterized by intense potassic, hematite, and moderate to strong carbonatization. Changes in alteration styles and intensities are observed with increasing proximity to the Douay Alkaline Intrusive Complex, indicating that the hydrothermal system is centered on the Douay Alkaline Intrusive Complex and corresponds to a magmatic-hydrothermal system.

The first facies are referred to the as the albitized facies. Consisting of quartz monzonite to monzonite intrusions. The albitized facies is interpreted as the oldest part of the Douay Alkaline

Intrusive Complex, displayed by crosscutting relationships of a later aplite dyke dated at 2690.1 ± 0.96 Ma (Mathieu et al., 2022). These intrusions are moderately to strongly altered by albitization, weak to moderate potassic, and carbonatization. The albitization is likely related to either the hydrolysis of alkali feldspar, the breakdown of plagioclase feldspar, or a Na- rich magmatic source (Kishida and Kerrich, 1987; Colvine et al., 1988; Witt, 1992; Smith et al., 1993; Gammons and Williams-Jones, 1995; McCuaig and Kerrich, 1998; Robert, 2001; Neumayr et al., 2008). Albitization is commonly observed as pervasive replacement in greenschist rocks and can be associated with gold mineralization in the Abitibi subprovince (Groves et al., 1998, Dubé and Gosselin, 2007). The contact between the albitized and hematized Groups are represented by a gradual colour change from red to pink to white, often referred to as “bleaching”. However, strongly albitized zones in the western Porphyry Zone tend to contain less gold than in the hematized facies (Fig. 2C).

The second facies are also of magmatic origin and appears as pink to dark red syenite intrusions (2676 +5/−6 Ma; Davis et al., 2000), known as the hematized facies. It is primarily composed of alkali feldspar phenocrysts with perthitic texture and minor interstitial quartz. The readily distinguishable hematized facies appears as a moderate to "brick” red colour and is represented by moderate to strong hematization and potassic alteration, often associated with gold mineralization. The distinctive “brick” red colour is due to very fine-grained hematite particles. This is due to the metasomatic replacement of the plagioclase by the alkali feldspar (Putnis et al., 2007). The pink-red color under cathodoluminescence is interpreted as alkali feldspar due to the Fe^{3+} enrichment known as the “alkali ferric iron effect”, which is generated by late fluids exsolved from the possible carbonatite or alkaline complexes (Elliott et al., 2018). The hematization and potassic alteration may be a result of early oxidizing fluids originating from the cooling intrusions of the latter syenite intrusions. Both the albitized and hematized facies are crosscut by small intervals of texturally destructive carbonatization.

The third facies, known as the carbonatized facies, represents small intervals (0.2–1 m) of grey to brown carbonatization. The carbonatized facies tends to be texturally destructive and mainly consists of Fe- to Mg-rich carbonates with inclusion-rich anhedral pyrites. The intense carbonatization could be linked to the amount of CO_2 produced by the alkaline complex during the crystallization process (Bailey and Hampton, 1990). The process of hydraulic fracturing induced enrichment of volatile elements such as significant input of CO_2 and elements such as Au, Ag, and Te, similar to the process at Lac Bachelor (Fayol and Jébrak, 2017). Alternatively, although less probable, the carbonatization could be attributed to a potential overprinting metamorphic event.

5.2. Gold Association with Oxidizing Fluids

The gold mineralization is spatially associated with the most altered intrusive rocks of the Douay Alkaline Intrusive Complex and tends to be associated with disseminated sulfide or associated with veinlets and breccias (Fig. 7&8a). The main alterations associated with the rocks of the Douay Alkaline Intrusive Complex are potassic metasomatism hematization, albitization, carbonatization, silicification, and minor sericitization (Fig. 10). Specifically, hematized facies tends to contain most of the disseminated gold mineralization (Fig. 2b), with small intervals overprinted by the carbonatized facies, which may locally increase gold grade. Barite is observed in the matrix and interstitial spaces of the hematized and carbonatized facies and within the pyrite grains as inclusions in the mineralized zones (Fig. 12a). Furthermore, the pyrite chemistry displays barium enrichments in both the core (Fig. 12a) and rims (Fig. 12c), implying magmatic oxidizing conditions throughout the crystallization of pyrite. The barium enrichments are specifically observed in both the hematized and late carbonatized facies pyrite grains. This implies the circulation of oxidizing fluids at the time of gold mineralization.

The Douay Alkaline Intrusive Complex exhibits a polymetallic signature. All facies display a moderate to strong correlation between Au and other elements such as Ag, Te, W, and Sb. All facies display a weak correlation present between Au and As (Fig. 14). Specifically, Te contents tend be higher in the pyrite grains from all facies within the Douay Alkaline Intrusive Complex, than those from typical orogenic gold style deposits (Fig. 15). Tellurium is soluble mainly in oxidized fluids that consist of a varying pH, low salinity, high temperature, and tends to concentrate during the vapour phase (Cook et al., 2009). Therefore, its solubility decreases in reduced conditions (Kelly et al 1998, Cooke and McPhail 2001, Cook et al., 2009, Scherbarth and Spry, 2006, Bruggers et al., 2012, Gao et al., 2017). Additionally, epithermal systems associated with alkali magmas tend to favor the movement of Te into the pyrite crystal structure, due to the alkaline magma having higher pH conditions (Gao et al 2017, Grundler et al., 2013, Smith et al., 2017). Consequently, Te in the pyrite structure may distort the lattice, potentially facilitating the incorporation of Au into the pyrite crystal lattice. This is supported by the findings of Cook et al. (2009) and Ciobanu (2012), who investigated As-free sulfides such as those analyzed at the Wasamac deposit by Mériaud and Jébrak (2017). Therefore, this indicates that As may not be necessary for gold incorporation into the pyrite lattice. The moderate to strong correlation between Te and Au, and lack of a correlation with As in the albitized, hematized, and carbonatized facies, along with the abundance of sulfate (barite and anhydrite) presents strong evidence of gold-rich oxidizing magmatic fluids.

5.3 Comparison between Douay and other gold deposits in the Northern Abitibi Subprovince

The Abitibi subprovince contains numerous gold deposits that show characteristics of IRGS, OGS, or show IRGS overprinted by OGS. The chemistry of pyrite from Douay is compared with data from over 1,000 pyrite analyses across 18 well-studied gold deposits, including the Vezza orogenic gold deposit. The comparison uses the 25th to 75th percentile envelope defined by Genna et al.

(2020) and Gaboury et al. (2021). The Douay deposit (blue) plots between the intrusion-related deposits end member, with greater than 65% SiO_2 (gray) and those with less than 65% SiO_2 (Fig 15).

This finding is further supported by the assays of mineralized samples (n=17) at Douay (Au > 300 ppb), which show an Au/Ag ratio of 1.5, indicating a magmatic-hydrothermal source for the mineralizing fluids. Typically, orogenic gold deposits have Au/Ag ratios between 5 and 10 (Dubé and Gosselin, 2007) whereas, Au/Ag ratios less than 5 are characteristic of deposits influenced by hydrothermal-magmatic fluids (Augustin & Gaboury, 2019).

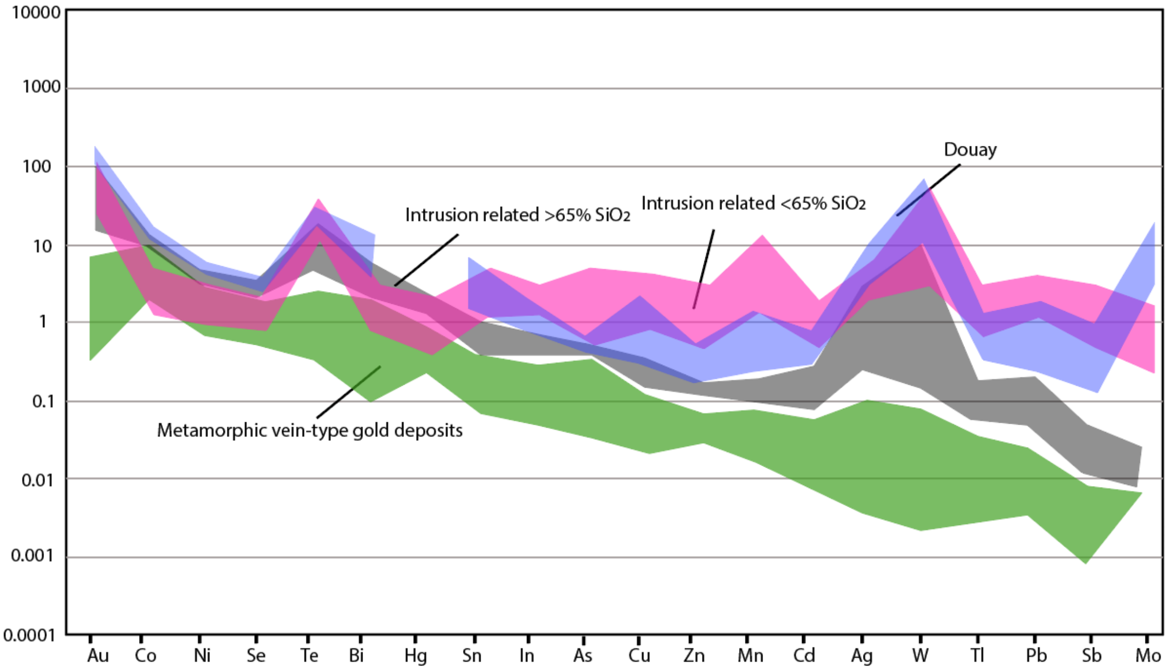

Figure 15: Classification patterns for orogenic gold deposits in the Abitibi greenstone belt, based on over 1000 pyrite analyses from 18 extensively studied gold deposits, using a 25th-75th percentile envelope. The Douay deposit (blue) plots between the intrusion-related deposits with greater than 65% SiO_2 (gray) and those with less than 65% SiO_2 (modified from Gaboury et al., 2021 à Perron Gold deposit).

Specifically, in the northern Abitibi subprovince, many gold deposits show characteristics of IRGS, OGS, or show IRGS overprinted by OGS. Intrusive bodies such as the Boyvinet stock on the Lac Shortt property and the O'Brien pluton at Lac Bachelor share similar characteristics with the Douay deposits. In contrast, the Vezza deposit, also situated along the east-west trending Casa Berardi

Tectonic Zone (CBTZ), exhibits very different characteristics and is more similar to orogenic gold systems (OGS).

The Vezza gold deposit is located within close proximity to the Casa Berardi Tectonic Zone (CBTZ) and is hosted in steeply dipping structures (striking east-west, dipping steeply to the south) that occur within the clastic sediments of the Taibi Group (Bouchard, 2017). The mineralization is located within a network of quartz-carbonate veinlets with minor tourmaline, and in replacement in iron formations and greywackes (Bouchard, 2017). Also, minor felsic intrusions have been observed containing minor amounts of gold mineralization (Bouchard, 2017). The gold mineralization tends to have a strong correlation with As (Bouchard, 2017). Therefore, the deposit is interpreted to have formed by the metamorphic devolatilization of the clastic sediments and basalts producing CO_2 rich reducing fluids (Bouchard, 2017).

The Vezza gold deposits shows similar characteristics to typical orogenic deposits, such as structurally controlled mineralization hosted in quartz-carbonate with minor tourmaline veins, along with extensive silicification and carbonatization alteration. These characteristics are very different from the gold mineralization observed in the Western Porphyry Zone at Douay deposit, where the gold is mainly hosted in finely disseminated pyrite hosted in the massive to porphyritic texture of hematized facies, which presents a weak correlation with As. Although the mineralization hosted in the Douay Alkaline Intrusive Complex is structurally controlled and primarily associated with disseminated sulphides, the general lack of quartz-carbonate veining and extensive silicification suggests that the mineralization is related to a magmatic fluid source.

The Lac Bachelor deposit is hosted within the O'Brien and East Sullivan intrusions, which are composed of quartz-syenite to alkali-granite (Fayol and Jébrak, 2017). The gold mineralization tends to be associated with disseminated pyrite in a magnetite-rich syenite, accompanied by fluorine-rich alkaline and hematite-rich metasomatized zones (Fayol and Jébrak, 2017). Minor gold mineralization is also present along the edges of the syenitic complex, contained in stockwork-like quartz veins (Fayol and Jébrak, 2017). Specifically, in the O'Brien pluton, and sulfate minerals such as barite and anhydrite occur in the metasomatized ore zones. The presence of purple fluorite and sulfate minerals is similar to the hematized facies located in the western porphyry zone.

The Boyvinet stock is comprised of monzodiorite and monzonite intrusive phases, which displays a polymetallic signature (Bi-Te-Cu-Ag-Sb; Côté-Lavoie, 2016). The intrusive body is strongly altered by intense alkali metasomatism, similar to the albitized and hematized facies observed in the Western Porphyry Zone at Douay. At Boyvinet, gold mineralization is linked to pyrite in later stages, suggesting that the IRGS may have contained less gold than the overprinting OGS (Côté-Lavoie, 2016, Mathieu, 2021). This implies that the Boyvinet stock could have served as a structural trap for magmatic and possible later metamorphic fluids due to its brittle nature (Côté-Lavoie, 2016, Mathieu, 2021).

We propose new discrimination diagrams, based on the chemistry of pyrite (Fig.16), where orogenic deposits are generally enriched in As and Sb, due to the devolatilization of sedimentary basins (Pitcairn et al., 2021), and IRGS are enriched in Te and Ag when the fluid is generated from a magmatic source (Mathieu, 2021). When we compare all the deposits using the binary diagram Sb-Ag, most of the data points for the albitized, hematized, and carbonatized pyrite chemistry samples plot on the intrusion-related field and overlap with pyrite from the Lac Bachelor deposit and Boyvinet stock fields suggesting the mineralizing fluids were generated from a magmatic source. Similarly, when comparing all the deposits using the binary diagram Te-As, most of the data points for the albitized, hematized, and carbonatized pyrite chemistry samples plot on the intrusion-related field and overlap with the pyrites from the Lac Bachelor deposit and Boyvinet stock fields. Although, some data points of the hematized and carbonatized facies overlap with the Vezza deposit field. This may be due to the increase in As due to the volatile phase of the alkaline intrusion.

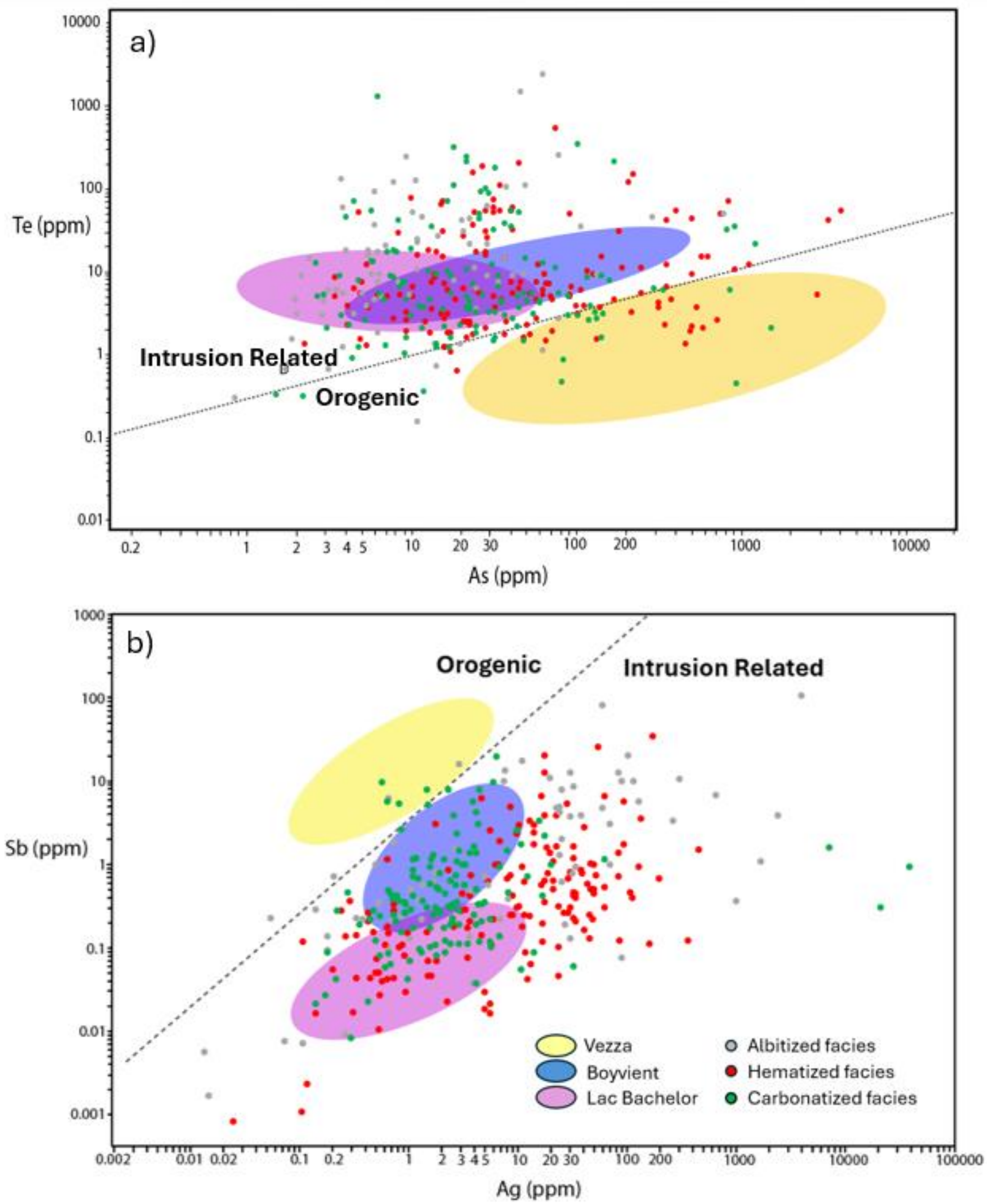

Figure 16: Proposed discrimination diagrams, based on the chemistry of pyrite. The fields are generated by Mahalanobis Ellipse (P=0.5) of Vezza (yellow; Bouchard, 2017), Boyvinet (blue; Côté-Lavoie, 2016), and Lac Bachelor (purple; Fayol and Jébrak, 2017) with pyrite chemistry results from the albitized, hematized, and carbonatized facies samples from the Douay Alkaline Intrusive Complex; (a): Te-As, (b) Sb-Ag.

CHAPTER 6: CONCLUSION

The relationship between gold mineralization and syn- to post-tectonic alkaline intrusions in the Abitibi subprovince has been a subject of ongoing debate. The Douay gold deposit exemplifies this controversy, as its gold mineralization is spatially linked to the multiphase Douay Alkaline Intrusion Complex. However, the deposit is also structurally controlled, raising the possibility that it could represent an intrusion-hosted orogenic gold system.

The Douay Alkaline Intrusive Complex originated from multiple magmatic pulses, which were formed by a low degree of partial melting and fractional crystallization. These processes allowed the separation of a highly evolved grey quartz monzonite to monzonite (albitized facies) and latter brick red to pink gold-rich syenite to monzonite intrusions (hematized facies) to evolve. Due to its low viscosity and fluorine enrichment, the alkaline magmas utilized deep pre-existing local or regional fault structures (e.g Casa Berardi Tectonic Zone) as conduits to emplace in shallow levels of the earths crust. As the intrusive body was emplaced and subsequently cooled along existing fault structures at shallow crustal levels, the shallow depth overpressures created hydraulic fracturing around and within the intrusive body. The process of hydraulic fracturing induced the enrichment of volatile elements such as a significant input of CO_2, and elements such as Au, Ag, and Te.

In conclusion, this study provides insights into the geological characteristics of the Douay Gold deposit, with a focus on the western portion of the Porphyry Zone. The results aid and develop our understanding of Neoarchean mineralizing systems, particularly those associated or spatially related to alkaline intrusions. Furthermore, this work has important implications for gold exploration, emphasizing the integration of structural controls and the contribution of both metamorphic and magmatic fluids in the genesis of gold deposits in the Abitibi subprovince.

REFERENCES

Augustin, J., & Gaboury, D. (2019). Multi-stage and multi-sourced fluid and gold in the formation of orogenic gold deposits in the world-class Mana district of Burkina Faso - Revealed by LA-ICP-MS analysis of pyrites and arsenopyrites. *Ore Geology Reviews*, *104*, 495–521. https://doi.org/10.1016/j.oregeorev.2018.11.011

Azevedo, C., Jébrak, M., Genna, D., & Pinti, D. L. (2022). Evidence of gold related to Neoarchean alkaline magmatism in the Abitibi greenstone belt (Canada) from mineral parageneses and microscale trace element geochemistry on pyrite. *Ore Geology Reviews*, *145*. https://doi.org/10.1016/j.oregeorev.2022.104878

Ayer, J., Amelin, Y., Corfu, F., Kamo, S., Ketchum, J., Kwok, K., & Trowell, N. (2002). Evolution of the southern Abitibi greenstone belt based on U-Pb geochronology: autochthonous volcanic construction followed by plutonism, regional deformation and sedimentation. *Precambrian Research*, *115*(1), 63–95. https://doi.org/10.1016/S0301-9268(02)00006-2

Bailey D K, & Hampton C M. (1990). Volatiles in alkaline magmatism. *Lithos*, *26*(1-2), 157–165. https://doi.org/10.1016/0024-4937(90)90045-3

Bigot, L., & Jébrak, M. (2015). Gold mineralization at the syenite-hosted Beattie gold deposit, Duparquet, Neoarchean Abitibi Belt, Canada. *Economic Geology and the Bulletin of the Society of Economic Geologists*, *110*(2), 315–335. https://doi.org/10.2113/econgeo.110.2.315

Bouchard, Maxime. (2017). *Caractérisation, facteurs de contrôle et métallogénie du dépôt aurifère atypique Vezza, zone de déformation de Douay, Matagami, Québec* [Dissertation]. https://constellation.uqac.ca/id/eprint/4236/

Brugger, J., Etschmann, B. E., Grundler, P. V., Liu, W., Testemale, D., & Pring, A. (2012). XAS evidence for the stability of polytellurides in hydrothermal fluids up to 599 °C, 800 bar. *American Mineralogist*, *97*(8-9), 1519–1522. https://doi.org/10.2138/am.2012.4167

Ciobanu, C. L., Cook, N. J., Utsunomiya, S., Kogagwa, M., Green, L., Gilbert, S., & Wade, B. (2012). Gold-telluride nanoparticles revealed in arsenic-free pyrite. *American Mineralogist*, *97*(8-9), 1515–1518. https://doi.org/10.2138/am.2012.4207

Colvine, A. C., & Commission géologique de l'Ontario. (1988). *Archean lode gold deposits in Ontario*. Ontario Geological Survey, Ministry of Northern Development and Mines.

Cook, N. J., Ciobanu, C. L., Spry, P. G., & Voudouris, P. (2009). Understanding gold-(silver)-telluride-(selenide) mineral deposits. *Episodes Journal of International Geoscience*, *32*(4), 249-263. https://www.researchgate.net/publication/259791380

Côté-Lavoie, Édouard. (2016). *Métallogénie et processus minéralisateurs du Stock de Boyvinet, Desmaraisville, Abitibi, Québec* [Dissertation]. https://constellation.uqac.ca/id/eprint/4023/

Cullers, R. L., & Graf, J. L. (1984a). Rare earth elements in igneous rocks of the continental crust: predominantly basic and ultrabasic rocks. In *Developments in geochemistry* (Vol. 2, pp. 237-274). Elsevier. https://doi.org/10.1016/B978-0-444-42148-7.50012-5

Cullers, R. L., & Graf, J. L. (1984b). Rare earth elements in igneous rocks of the continental crust: intermediate and silicic rocks–ore petrogenesis. In *Developments in geochemistry* (Vol. 2, pp. 275-316). Elsevier. https://doi.org/10.1016/B978-0-444-42148-7.50013-7

Daigneault, R., St-Julien, P., & Allard, G. O. (n.d.). Tectonic evolution of the northeast portion of the Archean Abitibi greenstone belt, Chibougamau area, Quebec. *Canadian Journal of Earth Sciences*, *27*(12), 1714–1736. https://doi.org/10.1139/e90-178

Davis, D. W., & Québec (Province). Ministère des ressources naturelles et de la faune. (2005). *Datations U-Pb effectuées en support aux travaux de cartographie géologique et de compilation géoscientifique du SGNO (2003-2004)*. Ressources naturelles et faune Québec. http://collections.banq.qc.ca/ark:/52327/45461

Davis, W. J., Lacroix, S., Gariépy, C., & Machado, N. (2000). Geochronology and radiogenic isotope geochemistry of plutonic rocks from the central Abitibi Subprovince; significance to the internal subdivision and plutono-tectonic evolution of the Abitibi Belt. *Canadian Journal of Earth Sciences = Revue Canadienne Des Sciences de La Terre*, *37*(2-3), 117–133. https://doi.org/10.1139/e99-093

De Souza, S., Dubé, B., McNicoll, V., Dupuis, C. D., Mercier-Langevin, P., Creaser, R. A. & Kjarsgaard, I. M. (2015). Geology, hydrothermal alteration, and genesis of the world-class Canadian Malartic stockwork-disseminated Archean gold deposit, Abitibi, Quebec. *Geological Survey of Canada, Open File*, 7852. https://doi.org/10.4095/296633

De Souza S., Dube B., Mercier-Langevin P., Dupuis C., McNicoll V., & Kjarsgaard I. (2019). Hydrothermal alteration mineralogy and geochemistry of the Archean world-class Canadian malartic disseminated-stockwork gold deposit, southern Abitibi Greenstone Belt, Quebec, Canada. *Economic Geology*, *114*(6), 1057–1094. https://doi.org/10.5382/econgeo.4674

Deditius, A. P., & Reich, M. (2016). Constraints on the solid solubility of Hg, Tl, and Cd in arsenian pyrite. *American Mineralogist*, *101*(6), 1451–1459. https://doi.org/10.2138/am-2016-5603

Dingwell, D. B., & Scarfe, C. M. (1985). Chemical diffusion of fluorine in melts in the system Na2OAl2O3SiO2. *Earth and Planetary Science Letters*, *73*(2-4), 377–384. https://doi.org/10.1016/0012-821X(85)90085-8

Dubé, B. & Gosselin, P. (2007). Greenstone-hosted quartz-carbonate vein deposits. *Geological Association of Canada, Mineral Deposits Division, Special Publication*, 5, 49-73.

Dubé, B., & Mercier-Langevin, P. (2020). Gold deposits of the Archean Abitibi greenstone belt, Canada. https://doi.org/10.5382/SP.23.32

Elliott, H. A. L., Wall, F., Chakhmouradian, A. R., Siegfried, P. R., Dahlgren, S., Weatherley, S., Finch, A. A., Marks, M. A. W., Dowman, E., & Deady, E. (2018). Fenites associated with carbonatite complexes: A review. *Ore Geology Reviews*, *93*, 38–59. https://doi.org/10.1016/j.oregeorev.2017.12.003

Fayol, N., & Jébrak, M. (2017). Archean sanukitoid gold porphyry deposits; a new understanding and genetic model from the Lac Bachelor gold deposit, Abitibi, Canada. *Economic Geology and the Bulletin of the Society of Economic Geologists*, *112*(8), 1913–1936. https://doi.org/10.5382/econgeo.2017.4534

Gaboury, D., Genna, D., Trottier, J., Bouchard, M., Augustin, J., & Kelly, M. (2021). The Perron Gold Deposit, Archean Abitibi Belt, Canada: Exceptionally High-Grade Mineralization Related to Higher Gold-Carrying Capacity of Hydrocarbon-Rich Fluids. *Minerals*, *11*(10), 1066. https://doi.org/10.3390/min11101066

Gao, S., Xu, H., Li, S., Santosh, M., Zhang, D., Yang, L., & Quan, S. (2017). Hydrothermal alteration and ore-forming fluids associated with gold-tellurium mineralization in the Dongping gold deposit, China. *Ore Geology Reviews*, *80*, 166–184. https://doi.org/10.1016/j.oregeorev.2016.06.023

Garbe-Schönberg, D., & Müller, S. (2014). Nano-particulate pressed powder tablets for LA-ICP-MS. *Journal of Analytical Atomic Spectrometry*, *29*(6), 990–1000. https://doi.org/10.1039/c4ja00007b

Goldfarb, R. J., & Groves, D. I. (2015). Orogenic gold: Common or evolving fluid and metal sources through time. *Lithos*, *233*, 2–26. https://doi.org/10.1016/j.lithos.2015.07.011

Goldfarb, R. J., & Pitcairn, I. (2022). Orogenic gold: is a genetic association with magmatism realistic? *Mineralium Deposita : International Journal for Geology, Mineralogy and Geochemistry of Mineral Deposits*, *58*(1), 5–35. https://doi.org/10.1007/s00126-022-01146-8

Gosselin, M. (2020). Maple Gold Commences Induced Polarization Work to Test for potential Higher-Grade Gold Lenses. Available from https://maplegoldmines.com/index.php/en/news/2020/327-apleoldommencesnducedolarizationorktoestfor20200129102300

Groves, D. I., Goldfarb, R. J., Gebre-Mariam, M., Hagemann, S. G., & Robert, F. (n.d.). Orogenic gold deposits: A proposed classification in the context of their crustal distribution and relationship to other gold deposit types. *Ore Geology Reviews*, *13*(1), 7–27. https://doi.org/10.1016/S0169-1368(97)00012-7

Helt, K. M., Williams-Jones, A. E., Clark, J. R., Wing, B. A., & Wares, R. P. (2014). Constraints on the genesis of the Archean oxidized, intrusion-related Canadian Malartic gold deposit, Quebec, Canada. *Economic Geology and the Bulletin of the Society of Economic Geologists*, *109*(3), 713–735. https://doi.org/10.2113/econgeo.109.3.713

Hofmann, A.W. (1988). Chemical differentiation of the Earth: the relationship between mantle, continental crust, and oceanic crust. *Earth and Planetary Science Letters*, *90*(3), 297. https://doi.org/10.1016/0012-821X(88)90132-X

Ispolatov V., Lafrance B., Dube B., Creaser R., & Hamilton M. (2008). Geologie and structural setting of gold mineralization in the Kirkland Lake-Larder Lake gold belt, Ontario. *Economic Geology*, *103*(6), 1309–1340. https://doi.org/10.2113/gsecongeo.103.6.1309

Jemielita, R. A., Davis, D. W., Krogh, T. E., & Spooner, E. T. C. (1989). Chronological constraints on the origin of Archean lode gold deposits in the southern Superior Province from U/Pb isotopic analyses of hydrothermal rutile and titanite. In *Geological Society of America, 1989 annual meeting Abstracts with Programs-Geological Society of America* (Vol. 21, No. 6, p. 351).

Jochum, K. P., Nohl, U., Herwig, K., Lammel, E., Stoll, B., & Hofmann, A. W. (2005). GeoReM: A New Geochemical Database for Reference Materials and Isotopic Standards. *Geostandards and Geoanalytical Research*, *29*(3), 333–338. https://doi.org/10.1111/j.1751-908X.2005.tb00904.x

Jochum, K. P., Weis, U., Stoll, B., Kuzmin, D., Yang, Q., Raczek, I., Jacob, D. E., Stracke, A., Birbaum, K., Frick, D. A., Günther, D., & Enzweiler, J. (2011). Determination of Reference Values for NIST SRM 610-617 Glasses Following ISO Guidelines. *Geostandards and Geoanalytical Research*, *35*(4), 397–429. https://doi.org/10.1111/j.1751-908X.2011.00120.x

Kelley, K. D., Romberger, S. B., Beaty, D. W., Pontius, J. A., Snee, L. W., Stein, H. J., & Thompson, T. B. (1998). Geochemical and geochronological constraints on the genesis of Au-Te deposits at Cripple Creek, Colorado. *Economic Geology and the Bulletin of the Society of Economic Geologists*, *93*(7), 981–1012. https://doi.org/10.2113/gsecongeo.93.7.981

Kontak, D. J., Dubé, B., & Benham, W. R. (2008). The Upper Beaver project, Kirkland Lake area: Investigation of a syenite-associated copper-gold deposit with magnetite-epidote-feldspar alteration. *Summary of field work and other activities*, 12-11.

Legault, M., Gauthier, M., Jébrak, M., Davis, D. W., & Baillargeon, F. (n.d.). Evolution of the subaqueous to near-emergent Joutel volcanic complex, Northern Volcanic Zone, Abitibi Subprovince, Quebec, Canada. *Precambrian Research*, *115*(1), 187–221. https://doi.org/10.1016/S0301-9268(02)00010-4

Maple Gold Mines Ltd. (2021, October 4). *Maple Gold intersects bonanza grade gold including 334.0 g/t gold over 1.0 metre in the Porphyry Zone at Douay*. Maple Gold Mines. https://www.maplegoldmines.com/index.php/en/news/news-releases/2021/532%20mapleoldntersectsonanzaradeoldncluding3340g20211004070000

Mathieu, L. (2021). Intrusion-associated gold systems and multistage metallogenic processes in the Neoarchean Abitibi Greenstone Belt. *Minerals*, *11*(3), 261. https://doi.org/10.3390/min11030261

Mathieu, L., Wasuita, T. D., Sherlock, R., Speidel, F., Marsh, J. H., Dubé, B., & Côté-Mantha, O. (2022). Zircon from Altered Monzonite Rocks Provides Insights into Magmatic and Mineralizing Processes at the Douay Au Project, Abitibi Greenstone Belt. *Geosciences*, *12*(3), 114. https://doi.org/10.3390/geosciences12030114

McCuaig, T.C., and Kerrich, R. (1998). P-T-t-deformation-fluid characteristics of lode gold deposits: Evidence from alteration systematics. *Ore Geology Reviews*, *12*(6), 381–453. https://doi.org/10.1016/S0169-1368(98)80002-4

McNicoll, V., Goutier, J., & Québec (Province). Ministère des ressources naturelles et de la faune. (2008). *Trois datations U-Pb de la région du lac au Goéland, sous-province de l'Abitibi*. Ressources naturelles et faune Québec. http://collections.banq.qc.ca/ark:/52327/1563663

Mériaud, N., & Jébrak, M. (2017). From intrusion-related to orogenic mineralization: The Wasamac deposit, Abitibi Greenstone Belt, Canada. *Ore Geology Reviews*, *84*, 289–308. https://doi.org/10.1016/j.oregeorev.2017.01.021

Monecke, T., Mercier-Langevin, P., and Dubé, B. (2017a). Archean Base and Precious Metal Deposits, Southern Abitibi Greenstone Belt, Canada. Archean Base and Precious Metal Deposits, Southern Abitibi Greenstone Belt, Canada, 19. https://doi.org/10.5382/rev.19

Monecke, T., Mercier-langevin, P., Dubé, B., and Frieman, B.M. (2017b). Chapter 1 Geology of the Abitibi Greenstone Belt. : 7–49. https://doi.org/10.5382/Rev.19.01

Müller, D., Franz, L., Herzig, P. M., & Hunt, S. (n.d.). Potassic igneous rocks from the vicinity of epithermal gold mineralization, Lihir Island, Papua New Guinea. *Lithos*, *57*(2), 163–186. https://doi.org/10.1016/S0024-4937(01)00035-4

Nadeau, O., Stevenson, R., & Jébrak, M. (2014). The Archean magmatic-hydrothermal system of Lac Shortt (Au-REE), Abitibi, Canada: Insights from carbonate fingerprinting. *Chemical Geology*, *387*, 144–156. https://doi.org/10.1016/j.chemgeo.2014.08.021

Phillips, G.N., and Powell, R. (2010). Formation of gold deposits: a metamorphic devolatilization model. *Journal of Metamorphic Geology*, *28*(6), 689–718. https://doi.org/10.1111/j.1525-1314.2010.00887.x

Pilote P, Guha J, Daigneault R, Robert F, & Golightly J P. (1990). Contexte structural et mineralisations auriferes des gites Casa-Berardi, Abitibi, Quebec. *Canadian Journal of Earth Sciences*, *27*(12), 1672. https://doi-org.sbiproxy.uqac.ca/10.1139/e90-175

Pitcairn, I. K., Leventis, N., Beaudoin, G., Faure, S., Guilmette, C., & Dubé, B. (2021). A metasedimentary source of gold in Archean orogenic gold deposits. *Geology (Boulder)*, *49*(7), 862–866. https://doi.org/10.1130/G48587.1

Powell, W. G., Carmichael, D. M., & Hodgson, C. J. (1995). Conditions and timing of metamorphism in the southern Abitibi greenstone belt, Quebec. *Canadian Journal of Earth Sciences*, *32*(6), 787–805. https://doi.org/10.1139/e95-067

Putnis, A., Hinrichs, R., Putnis, C. V., Golla-Schindler, U., Collins, L. G., & theme session VGP8 of the annual European Geosciences Union General Assembly 32nd IGC Vienna Austria 20050425-20050427. (2007). Hematite in porous red-clouded feldspars: Evidence of large-scale crustal fluid-rock interaction. *Lithos*, *95*(1-2), 10–18. https://doi.org/10.1016/j.lithos.2006.07.004

El Rassi, D., Eng, P., Mccombe, D., and Evans, L. 2019. Techical Report on the Douay Gold Project, Northwestern Quebec, Canada NI 43-101. 1. CHECK

Robert, F. (2001). Syenite-associated disseminated gold deposits in the Abitibi greenstone belt, Canada. *Mineralium Deposita: International Journal of Geology, Mineralogy and Geochemistry of Mineral Deposits*, *36*(6), 503–516. https://doi.org/10.1007/s001260100186

Rowins, S. M., Cameron, E. M., Lalonde, A. E., & Ernst, R. E. (1993). Petrogenesis of the late Archean syenitic Murdock Creek Pluton, Kirkland Lake, Ontario; evidence for an extensional tectonic setting. *The Canadian Mineralogist*, *31*, 219–244. CM31_219.pdf

Savard, D., Bouchard-Boivin, B., Barnes, S. J., & Garbe-Schönberg, D. (2018, July). UQAC-FeS: A new series of base metal sulfide quality control reference material for LA-ICP-MS analysis. In *Proceedings of the 10th International Conference on the Analysis of Geological and Environmental Materials, Sydney, Australia* (pp. 8-13). https://doi.org/10.1111/j.1751-908X.2009.00003.x

Scherbarth, N. L., & Spry, P. G. (2006). Mineralogical, petrological, stable isotope, and fluid inclusion characteristics of the Tuvatu gold-silver telluride deposit, Fiji; comparisons with the Emperor Deposit. *Economic Geology and the Bulletin of the Society of Economic Geologists*, *101*(1), 135–158. https://doi.org/10.2113/gsecongeo.101.1.135

Fitz Gerald, J. D., & Stünitz, H. (1993). Deformation of granitoids at low metamorphic grade. I: Reactions and grain size reduction. *Tectonophysics*, *221*(3-4), 269–297. https://doi.org/10.1016/0040-1951(93)90163-E

Thurston, P. C., Ayer, J. A., Goutier, J., & Hamilton, M. A. (2008). Depositional gaps in Abitibi greenstone belt stratigraphy; a key to exploration for syngenetic mineralization. *Economic Geology and the Bulletin of the Society of Economic Geologists*, *103*(6), 1097–1134. https://doi.org/10.2113/gsecongeo.103.6.1097

Wilson, S. A., Ridley, W. I., & Koenig, A. E. (2002). Development of sulfide calibration standards for the laser ablation inductively coupled plasma mass spectrometry technique. *J. Anal. At. Spectrom.*, *17*(4), 406–409. https://doi.org/10.1039/B108787H

Winchester J A, & Floyd P A. (1977). Geochemical discrimination of different magma series and their differentiation products using immobile elements. *Chemical Geology*, *20*(4), 325–343. https://doi.org/10.1016/0009-2541(77)90057-2

W.K. Witt. (1992). Porphyry intrusions and albitites in the Bardoc-Kalgoorlie area, Western Australia, and their role in Archean epigenetic gold mineralization. *Canadian Journal of Earth Sciences*, *29*(8), 1609. https://doi.org/10.1139/e92-127

Zhang, J., Lin, S., Linnen, R., & Martin, R. (2014). Structural setting of the Young-Davidson syenite-hosted gold deposit in the Western Cadillac-Larder Lake Deformation Zone, Abitibi Greenstone Belt, Superior Province, Ontario. *Precambrian Research*, *248*, 39–59. https://doi.org/10.1016/j.precamres.2014.04.007

ANNEXES

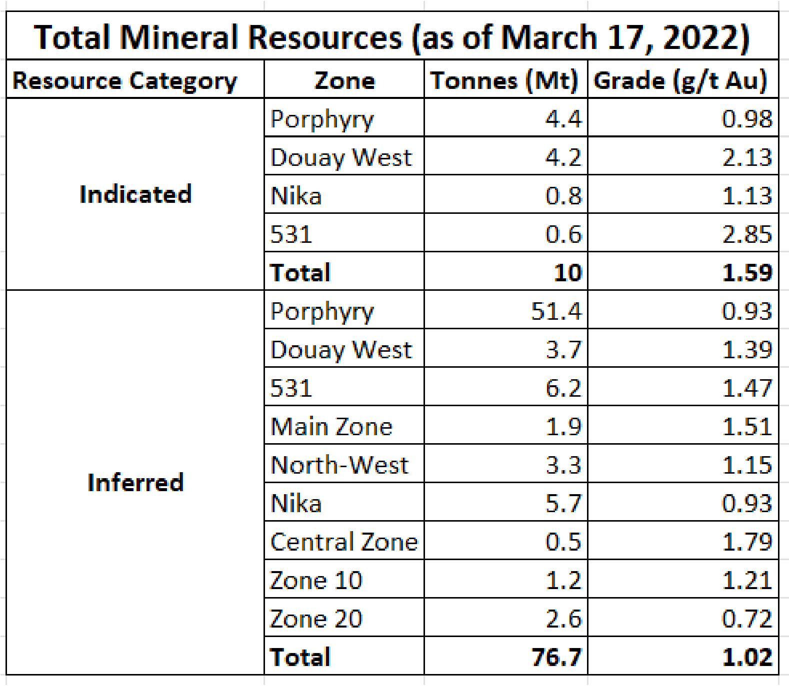

Total Mineral Resources (as of March 17, 2022)

Resource Category	Zone	Tonnes (Mt)	Grade (g/t Au)
Indicated	Porphyry	4.4	0.98
	Douay West	4.2	2.13
	Nika	0.8	1.13
	531	0.6	2.85
	Total	**10**	**1.59**
Inferred	Porphyry	51.4	0.93
	Douay West	3.7	1.39
	531	6.2	1.47
	Main Zone	1.9	1.51
	North-West	3.3	1.15
	Nika	5.7	0.93
	Central Zone	0.5	1.79
	Zone 10	1.2	1.21
	Zone 20	2.6	0.72
	Total	**76.7**	**1.02**

Annex 1: The total mineral resource estimation separated into indicated and inferred for each mineralized zone at the Douay Gold project.

Drillhole Number	UTM Northing	UTM Easting
DO-11-33	5490800.14	705870.49
DO-12-97	5490802.1	705900.08
DO-18-230	5490645	705899
DO-19-256	5491023	705937
DO-20-281	5490925	705934
DO-20-280	5491136	705870
DO-20-283	5491058	705948
DO-21-295	5491060	705950

Annex 2: Collar information for each drill hole that samples were taken from

Sample Number	**Drill Hole**	**Sample Depth (m)**	**Geochemistry Sample Type**	**Facies**	**EM**	**SEM**	**LA-ICP-MS**	**Mineral Analyzed**
G1	DO-20-230	103.10-104.10	Quarter Core	Volcanic				
G2	DO-19-256	85-86	Quarter Core	Carbonatized				
G3	DO-20-280	190.35-191.45	Quarter Core	Albitized				
G4	DO-20-281	136.5-137.5	Quarter Core	Hematized				
G5	DO-20-281	238-239	Quarter Core	Albitized				
G6	DO-12-97	201.60-202.90	Quarter Core	Volcanic				
G7	DO-11-33	379.10-380	Quarter Core	Albitized				
G8	DO-11-33	234.40-235.40	Quarter Core	Hematized				
G9	DO-20-281	149-150	Quarter Core	Hematized				
G10	DO-21-295	126.50-127.50	Quarter Core	Albitized				
G11	DO-11-33	261.50-262.50	Quarter Core	Albitized				
G12	DO-12-97	277.90-278.7	Quarter Core	Hematized				
TW-01	DO-12-97	28.5	PULP	Volcanic				
TW-02	DO-12-97	58.1	PULP	Volcanic				
TW-03	DO-12-97	83.7	PULP	Least Altered				
TW-03A	DO-12-97	86.2	PULP	Least Altered				
TW-04	DO-12-97	80.1	PULP	Least Altered	√	√		
TW-05	DO-12-97	261.6	PULP	Hematized	√	√	√	Pyrite/Carbonate/Feldspar

TW-05A	DO-12-97	266.1	PULP	Hematized	√	√	√	Pyrite/Carbonate/Feldspar
TW-06	DO-12-97	258.1	PULP	Hematized				
TW-07	DO-12-97	277.4	PULP	Hematized	√	√		
TW-08	DO-12-97	304.1	PULP	Least Altered				
TW-09	DO-12-97	314.5	PULP	Least Altered	√	√		
TW-10	DO-12-97	324.2	PULP	Hematized				
TW-11	DO-12-97	362.7	PULP	Albitized		√		
TW-12	DO-12-97	366.9	PULP	Albitized				
TW-13	DO-12-97	430.9	PULP	Albitized				
TW-14	DO-12-97	446.6	PULP	Albitized				
TW-15	DO-12-97	384.8	PULP	Albitized	√	√	√	Pyrite/Feldspar
TW-16	DO-12-97	244.2	PULP	Carbonatized				
TW-17	DO-12-97	233.5	PULP	Volcanic				
TW-18	DO-12-97	109.9	PULP	Hematized				
TW-19	DO-12-97	111.6	PULP	Volcanic	√		√	Pyrite/Carbonate
TW-20	DO-12-97	129.4	PULP	Albitized				
TW-21	DO-12-97	145.1	PULP	Volcanic				
TW-22	DO-12-97	209.3	PULP	Volcanic				
TW-23	DO-20-281	212.9	PULP	Albitized		√		
TW-24	DO-20-281	214	PULP	Albitized				

TW-25	DO-20-281	200.5	PULP	Albitized				
TW-26	DO-20-281	196.9	PULP	Albitized				
TW-27	DO-20-281	30.6	PULP	Volcanic				
TW-28	DO-20-281	64.1	PULP	Hematized				
TW-29	DO-20-281	110.6	PULP	Carbonatized			√	Pyrite
TW-30	DO-20-281	117.7	PULP	Hematized				
TW-31	DO-20-281	117.1	PULP	Carbonatized				
TW-32	DO-20-281	151.1	PULP	Least Altered				
TW-33	DO-20-281	255.5	PULP	Albitized				
TW-34	DO-19-256	59.5	PULP	Albitized		√	√	Pyrite
TW-35	DO-19-256	65.2	PULP	Carbonatized				
TW-36	DO-19-256	76.8	Thin Section only	Albitized				
TW-37	DO-19-256	85.6	PULP	Albitized				
TW-38	DO-19-256	167.7	PULP	Carbonatized			√	Pyrite
TW-39	DO-20-283	54.6	Thin Section Only	Carbonatized			√	Pyrite
TW-40	DO-20-283	61.3	Thin Section Only	Hematized				
TW-41	DO-20-283	114.1	Thin Section Only	Albitized				
TW-42	DO-20-283	159.3	Thin Section Only	Albitized				
TW-43	DO-20-283	188.9	Thin Section Only	Hematized			√	Pyrite/Carbonate
TW-44	DO-20-283	198.6	Thin Section Only	Albitized			√	Pyrite

TW-45	DO-11-33	39.2	Thin Section Only	Hematized				
TW-46	DO-11-33	58.9	Thin Section Only	Volcanic				
TW-47	DO-11-33	59.1	Thin Section Only	Volcanic				
TW-48	DO-11-33	75.9	Thin Section Only	Volcanic				
TW-49	DO-11-33	240.1	Thin Section Only	Hematized		√		
TW-50	DO-11-33	318.1	Thin Section Only	Albitized				
TW-51	DO-11-33	331.6	Thin Section Only	Albitized				
TW-52	DO-11-33	348.1	Thin Section Only	Albitized				
TW-53	DO-11-33	353.1	Thin Section Only	Albitized		√	√	Feldspar/Carbonate
TW-54	DO-11-33	377.2	Thin Section Only	Albitized				
TW-55	DO-20-280	64.6	Thin Section Only	Carbonatized				
TW-56	DO-20-280	82.9	Thin Section Only	Albitized				
TW-57	DO-20-280	164.3	Thin Section Only	Least Altered				
TW-58	DO-20-280	188.6	Thin Section Only	Albitized				
TW-58A	DO-20-280	195.8	Thin Section Only	Albitized				
TW-59	DO-20-280	222.3	Thin Section Only	Albitized				
TW-60	DO-20-280	200.8	Thin Section Only	Carbonatized	√	√		
TW-61	DO-20-280	309.7	Thin Section Only	Least Altered			√	Feldspar/Carbonate
TW-62	DO-20-280	288.6	Thin Section Only	Sedimentary		√		
TW-63	DO-19-256	80.4	Thin Section Only	Carbonatized			√	Pyrite

TW-64	DO-20-281	142.5	Thin Section Only	Albitized			√	Pyrite
TW-65	DO-20-281	123.6	Thin Section Only	Hematized			√	Pyrite
TW-66	DO-20-283	195.2	Thin Section Only	Albitized			√	Pyrite
TW-67	DO-20-283	299.1	Thin Section Only	Albitized				
TW-68	DO-11-33	244	Thin Section Only	Hematized			√	Pyrite
TW-69	DO-12-97	300.2	Thin Section Only	Hematized			√	Pyrite
TW-70	DO-11-33	263	Thin Section Only	Hematized			√	Pyrite
TW-71	DO-21-295	57.7	Thin Section Only	Hematized			√	Pyrite/Carbonate/Feldspar
TW-72	DO-21-295	59.5	Thin Section Only	Carbonatized Facies			√	Pyrite

Annex 3: A sample summary table indicating, which each of the 72 thin section samples and 40 geochemistry samples collected from 8 drill holes located in the Western Porphyry Zone.